2022-05-12

Tabletop Extreme-Ultraviolet Source Using High Harmonic Generation for Polarization Sensitive Imaging

Taylor Jordan Buckway
Brigham Young University

Tabletop Extreme-Ultraviolet Source Using High Harmonic Generation for Polarization Sensitive Imaging

Taylor Jordan Buckway

A thesis submitted to the faculty of
Brigham Young University
in partial fulfillment of the requirements for the degree of

Master of Science

Richard Sandberg, Advisor
Justin Peatross
Karine Chesnel

Department of Physics and Astronomy

Brigham Young University

ABSTRACT

Tabletop Extreme-Ultraviolet Source Using High Harmonic
Generation for Polarization Sensitive Imaging

Taylor Jordan Buckway
Department of Physics and Astronomy, BYU
Master of Science

We are developing a tabletop extreme-ultraviolet source using high harmonic generation at Brigham Young University. The thesis goes over the theory of high harmonic generation using the three-step model. This tabletop source was designed for probing magnetic domains of iron nanoparticles. We present optimization of the 42 eV and 52 eV harmonics through phase matching. Phase matching consists of tuning the intensity of the IR beam and pressure of the gas medium. The target gas medium used for this thesis is argon. The 42 eV harmonic was optimized to 8.2 billion photons per second. This was used with a 1500 mm focal-length lens, 15 mm medium length, laser power of 1.53 Watts, and a pressure of 12 Torr of argon gas. The 52 eV harmonic was optimized to 1.5 billion photons per second with a 1500 mm focal-length lens, 20 mm medium length, laser power of 3.29 W, and 14.9 Torr of argon gas. There are two designs for selection of harmonics: 1) a tunable design consisting of a toroidal mirror and flat diffraction grating and 2) a set of normal-incidence extreme-ultraviolet mirrors designed for 42 or 52 eV photons.

Magnetic imaging uses x-ray magnetic circular dichroism to obtain magnetic contrast and use it to visualize magnetic nanosystems. Therefore, the high harmonic source also needs to generate circularly polarized light. Generating circularly polarized high harmonics is possible with a bichromatic beam. This is achieved using an apparatus called the MAZEL-TOV designed by Oren Cohen's group at Technion University in Israel. The MAZEL-TOV consists of a BBO crystal for second harmonic generation, a pair of pulse delay compensation plates, and a quarter-wave plate. These optics are placed inline with the laser beam. We have successfully optimized the circularly polarized extreme-ultraviolet harmonics with the MAZEL-TOV. A spectrometer was made to calibrate the harmonics in the MAZEL-TOV spectrum. The tabletop source was then used to demonstrated coherent diffraction imaging of two pinholes.

Keywords: [High harmonic generation (HHG), MAZEL-TOV, phase matching, coherent diffraction imaging (CDI)]

ACKNOWLEDGMENTS

I want to acknowledge and thank many professors, students, and others who've been supportive and assisted in the completion of this work. Dr. Richard L. Sandberg who is my advisor and provided exceptional guidance throughout the work. Dr. Justin Peatross for helping me understand the theory of high harmonic generation and for the equipment he lent for the tabletop source. Dr. Karine Chesnel for helping me understand magnetic materials for which we will study with the developed tabletop source. Dr. David Allred for helping me understand and set up equipment used in the EUV source and for providing incite in the results concerning the M-edge of iron. Graduate student J. Nicholas Porter for developing the code to automate stages and cameras used for imaging. Graduate student Daniel Hodge for collaboration of coherent diffraction imaging. Many undergraduate students including William Giforos, Nathan Blanchard, Maeser Flake, Jacob Feltman, Aaron Redd, and Corbin Maciel who have all assisted with the set up of the tabletop source and collection of data. I want to thank my wife, Desiree, who has been very supportive in my work and in whom I will always love and appreciate. Lastly, my Heavenly Father who has opened the door and gave me the knowledge and capability to accomplish the work.

Contents

Table of Contents **iv**

List of Figures **vi**

List of Tables **xii**

1 Introduction **1**

2 High Harmonic Generation **5**
2.1 Step 1: Ionization of the Electron 6
2.2 Step 2: Acceleration of Free Electron in the External Electric Field 7
2.3 Step 3: Recombination of Electron with Parent Ion 10
2.4 Phase Matching 12
2.4.1 Types of Phase Mismatch 13
2.5 Coherence of High Harmonics 15
2.5.1 Spatial Coherence 15
2.5.2 Temporal Coherence 16

3 Coherent Diffraction Imaging **18**
3.1 Theory of Diffraction 18
3.2 Oversampling the Diffraction Pattern 19
3.3 Phase Retrieval Algorithms 20

4 EUV Source Design **22**
4.1 Tunable Harmonics Design 24
4.1.1 Toroidal Mirror 24
4.1.2 Diffraction Grating 26
4.2 Normal-incidence EUV Mirrors Design 28
4.3 Ti:Sapphire Laser 29
4.4 MAZEL-TOV 29
4.4.1 BBO Crystal 32
4.4.2 Calcite Plates 32

4.4.3 Quarter-wave Plate and Optical Window 34

5 Experimental Set Up and Results of the Tabletop EUV Source 35
5.1 Optimization the Harmonics 35
5.1.1 Optimization of the 42 eV Harmonic 36
5.1.2 Optimization of the 52 eV Harmonics 40
5.2 Results for MAZEL-TOV 42
5.3 Reconstruction of the Two Pinhole Diffraction 48

6 Conclusion 52

Appendix A Physical Constants and Useful Relations 54

Appendix B Phase Retrieval Algorithms 55
B.1 Error Reduction Algorithm 56
B.2 Hybrid Input-Output 56
B.3 Shrinkwrap 57
B.4 Code Used for Reconstruction of Images for this Thesis 57

Appendix C EUV Mirrors Reflection Curves 61

Appendix D Transmission Tables for Aluminum Filters 63

Appendix E Processing Two Pinhole Diffraction Pattern and Reconstruction 66

Bibliography 68

List of Figures

1.1 Dichroism effects of ferromagnetic and antiferromagnetic materials. Left plot shows circular dichroism effects of ferromagnet, iron. Right plot shows linear dicroism effect of antiferromagnet, perovskite oxide. Taken from [1]. 3

2.1 (A) High harmonic spectrum measured on our system with an EUV sensitive CCD camera. Only odd harmonics are generated with a monochromatic beam. The harmonics are integer multiples of the IR photon energy (1.55 eV). (B) Diagram of the semi-classical three-step model of the HHG process to produce EUV photons [2]. The process involves the ionization of the electron from the parent atom, acceleration of the electron in the electric field of driving laser, and recombination of the electron with the parent atom generating an EUV photon. (B) was taken from [3]. 6

2.2 Electric field (blue) of a 35 fsec laser pulse. It is oscillating thus the electrons will round trip back to the parent ion. Intensity (red) is proportional to the square of the electric field, $I \propto |E_0|^2$. 8

2.3 Motion of a free electron as it travels in an external electric field of the laser. Each line represents the phase of the laser's electric field where the electron is ionized. The dashed line represents the position of the atom. The laser field phase of 18°corresponds to the trajectory where the electron approaches the parent ion with the maximum kinetic energy. Note that for some initial phase positions, the electron trajectory never returns to the position of the ion. 9

2.4 Return energies for different initial phases. The maximum has a value of $3.17U_p$ which is where the highest harmonics are generated. This corresponds to an initial phase of 18°. 10

2.5 Observed harmonics spectra for several nobles gases and wavelengths of driving laser. Taken from [4]. 11

2.6 Measurements of the spatial coherence of the generated EUV light using two pinhole diffraction. Different pinhole separations were used to obtain each image. The fringe visibility is very high which indicates that HHG produces highly spatially coherent EUV beams. Taken from [5]. 16

3.1 Demonstration of the basic principles of iterative phase retrieval knowns as error reduction developed by Fienup [6]. The square root of the measured diffraction pattern in the detector plane is assigned an initial random phase. This is the detector plane that initialises the iterative phase retrieval. This detector wave is then propagated back to the sample plane via an inverse Fourier transform where the compact support constraint is applied. This modified wave is propagated back to the detector plane where an error is computed and the amplitude constraint is applied again, but the phase is allowed to remain. This process continues until the error is reduced and the phases and images converge. Taken from [7]. 21

4.1 (A) Design of the tabletop EUV source for magnetic imaging, consisting of a Solstice Ace Ti:sapphire amplifier, MAZEL-TOV apparatus, a vacuum system, argon gas cell, and two separate optical designs for selecting harmonics.(B) An image of the tabletop source. (C) An image of the EUV normal-incidence mirror design for selecting a harmonic. (D) The IR beam is focused into a gas cell containing argon gas around 20 Torr pressure where the high harmonics are generated. The IR beam is blocked by two aluminum filters placed in series. The EUV beam transfers through the aluminum filters. The desired harmonic is selected either by normal-incidence EUV mirrors or a toroidal mirror and grating pair. The selected harmonic is then used to probe the sample. (E) The system also contains the insertable MAZEL-TOV apparatus. This allows full polarization tunability between linear and circular polarization. It is important to note that the MAZEL-TOV may not work with the tunable spectrometer since the EUV beam will be at grazing incidence for each optic. This can alter the polarization of the beam. 23

4.2 Toroidal mirror graphic. It displays the radii of curvature with identified tangential and sagittal planes. Taken from [8]. 24

4.3 Diagram of the function of the diffraction grating. The grating will separate the harmonics into individual beam as described by equation 4.4 27

4.4 Measured reflection curves for the two sets of EUV mirrors. One is designed for 41.85 eV and the other is designed for 52 eV wavelengths. These mirrors are designed to reflect at angle of 5^o normal-incidence. 28

4.5 Threefold pattern of the electric field polarization formed through the combination of IR (left circular) with its second harmonic (right circular). The IR and blue beams are circularly polarized and have opposite helicities. An electric field with this pattern generates circularly polarized high harmonics. 30

4.6 Diagram describing how left circularly polarized IR photons combined with right circularly polarized blue photons to generate either a right or left circularly polarized EUV beam. The conservation of energy requires that the generated EUV photon energy is the sum of the number of IR and blue photons energies. Angular momentum conservation requires the difference in number of IR to blue photons to be ± 1. 31

4.7 Schematic of the MAZEL-TOV apparatus. The o-polarized IR beam is converted to a bichromatic circularly polarized beam which is used to generate circularly polarized high harmonics. Top picture of the MAZEL-TOV apparatus is included. . 31

4.8 Diagram of the functionality of a calcite plate. The group velocity mismatch between the IR and blue pulse is corrected as they pass through the plate. The IR beam is aligned along the ordinary plane of the crystal while the blue beam is aligned along the extraordinary plane. The optical axis makes an angle of 55^o from the normal axis to the surface of the crystal. Tilting the calcite crystal adjusts the extraordinary index of refraction which varies the group velocity of the blue pulse. 33

5.1 Three dimensional plot of 42 eV photon counts per second with dependence on the output power of the laser and pressure of the argon gas. This was done with a medium length of 10 mm and lens of focal-length 1000 mm. The optimal phase matching conditions favor a power of 3.36 Watts with gas pressure of 26 Torr. . . . 37

5.2 Two dimensional plot of the pressure power study. This shows that the phase matching tends to favor from 26 to 28 Torr for different powers. 38

5.3 Beam profiles at different pressures with power set at 3.36 Watts. We used a 10 mm medium length and 1000 mm focal-length lens. The images were scaled to the maximum value in the 26 Torr image. Each image reports the pressure and the number of photons per second detected on the CCD camera. 38

5.4 Plot of the number of photons per second for different medium lengths. The plot shows a 15 mm medium length is optimal for 42 eV harmonics. This data was obtain while using a 1500 mm lens. 39

5.5 Beam profile of the optimized 42 eV beam. A medium length of 15 mm with a lens focal-length of 1500 mm was used with this data set. The number of photon counts is 1.5 billion photons per second. Two 0.2 micron aluminum filters were used to take this data. If 0.1 micron filters are used instead, the total photons would be approximately 8.1 billion per second. 40

5.6 Beam profile of the 52 eV harmonic. A medium length of 20 mm with a lens focal-length of 1500 mm was used with this data set. The measured value was 283 million photons per second. Two 0.2 micron aluminum filters were used to take this data. If 0.1 micron filters are used instead the total photons would be approximately 1.5 billion per second. 41

5.7 Beam profile of 52 eV harmonic that will be used for experiments in magnetic imaging. The parameters were 3.6 Watts with a 1000 mm lens, 7 mm medium length, and 27 Torr gas pressure. The number of photons per second measured onto the CCD detector was 581 million. 42

5.8 Plot of group delay compensation versus angle of incidence of one calcite plate. The plot is fitted to an equation of a line, $Delay = 16\frac{fsec}{degree}AOI + 450fsec$. Taken from Ekmsa Optics [9]. 43

5.9 Generated circularly polarized harmonics spectrum from the MAZEL-TOV. (A) The image of the harmonic spectrum. (B) Two dimensional plot of the image with the total photon counts per second for each identified harmonic. As can be seen, there are harmonic pairs where every third harmonic is suppressed. Each pair consists of one right and one left circularly polarized beam [10, 11]. 45

5.10 (A) Combined circular and linear spectra of the high harmonic source. The linear spectrum (red) was generated using typical high harmonic methods which only generates linearly polarized light. The circular or MAZEL-TOV spectrum (purple) shows odd and even harmonics with every third harmonic suppressed. Comparison of the two spectra reveals which of the harmonics of the circular spectrum are odd. An arrow is drawn showing a suppressed odd harmonic that must be the 21^{st}, 27^{th}, or 33^{rd} harmonic. (B) Normalized curves of circular and linear spectra with transmission curves. Data for transmission curves taken from CXRO x-ray database [12] and then interpolated to the spectra. 47

5.11 Measured diffraction signal of two 10 micron pineholes separated by a distance of 40 microns. This diffraction pattern is used to reconstruct the pinholes with CDI. The visibility of the fringes indicates that the generate 42 eV harmonics has high spatial coherence. The signal is log scaled to show the outer rings. A description of how the data was processed can be found in appendix E 49

5.12 Reconstruction of the two pinhole diffraction pattern. The OS was calculated to be 7.2. (A) shows the reconstructed pinholes and (B) is the retrieved phase of the pinholes. 50

5.13 Two pinhole measurements. (A) Pinholes measured under a microscope. They are about 10 microns in diameter with 40 micron seperation. (B) Image of the reconstructed pinholes. (C) is the two dimensional plot of the reconstructed pinholes with the measured values. Measurements of the reconstructed pinholes were found by considering the FWHM of each peak. One peak is greater than the other which indicates that the right peak was more brightly illuminated by the EUV beam. . . . 51

6.1 Diagram of diffraction from a magnetic sample. The diffraction pattern would contain a dim circular speckle pattern surrounding the central diffraction pattern. The speckle pattern contains information of the magnetic domains. This image was altered and taken from [1]. 53

C.1 Measured reflections of the 42 eV mirrors. 61

C.2 Measured reflections of 52 eV mirrors. 62

E.1 Images of the data (A) before and (B) after processing preparatory for reconstruction. There is a background gradient coming from the scattered EUV beam in image (A) which needed to be removed for CDI to work properly. 66

E.2 Linear threshold created using a combination of X and Y gradient images. This was used to threshold the pinhole data to minimize the gradient noise. The values of the Y gradient are three times more than the X gradient. The linear gradient still needed to be combined with a flat threshold else another gradient background is formed in the image. 67

List of Tables

4.1 Radii curvatures of the toroidal mirrors from ARW Optical. They are designed to reflect at 10^o grazing incidence to minimize astigmatism. Reflections of the 52.7 eV harmonics from gold surface mirrors will be approximately 67% [12] 26

D.1 Filter transmission for 42 eV light. This is used to compare how much light is transmitted with different configurations of filters. The combinations such as 1-0.2 then 1-0.1 read one 0.2 micron filter then one 0.1 micron filter. When the CCD camera was saturated, a thicker filter was used to prevent saturation. This data table help estimate how many photons per second hit the CCD camera if thinner filters were used. This was primarily used to optimization of HHG. 64

D.2 Filter transmission for 52 eV light. This is used to compare how much light is transmitted with different configurations of filters. The combinations such as 1-0.2 then 1-0.1 read one 0.2 micron filter then one 0.1 micron filter. When the CCD camera was saturated, a thicker filter was used to prevent saturation. This data table help estimate how many photons per second hit the CCD camera if thinner filters were used. This was primarily used to optimization of HHG. 65

Chapter 1

Introduction

Polarization sensitive imaging with x-rays has been performed primarily at large photon sources such as synchrotrons and free electron lasers. These sources produce bright x-ray beams with tunable photon energy and polarization by using insertion devices knows as undulators [13]. Polarization control is an especially powerful aspect of these sources which can be used to image systems such as chirality in biological systems and domain formation in correlated electron materials (such as ferroelectric or magnetic domains). However, some nanoscale magnetic systems are best investigated at larger nanoscale wavelengths, a region of the electromagnetic specrum still to explore for magnetic imaging. To help fill the gap, we have developed a tabletop source of coherent extreme-ultraviolet (EUV) pulses at Brigham Young University. This source is based on ultrafast laser high harmonic generation (HHG) and is suitable for studying nanometer scale and ultrafast dynamics. In this introduction, I will review some basic concepts of magnetism which will provide motivation in developing a EUV tabletop source with a full range of polarization control.

Magnetic materials such as magnetite have been objects of interest for a few thousand years. The first technologies developed using magnets were compasses which assisted sailors. For the past 400 years, scientist have investigated the connection between magnetism and electricity, leading to revolutionary technologies such as power generators, data storage, and undulators for synchrotrons

and free electron lasers [1]. These transformative advancements motivate scientists to continue research on magnetism in hopes of improving data storage, superconductor technology, and creating spintronics [1, 14]. Critical to many of these technologies is the dynamics of the magnetic ordering at the nanoscale. Also critical to faster, potentially future data storage application is the ultrafast ordering of the electron spins in the materials [15, 16].

Imaging of magnetic materials has been conducted for several decades at synchrotrons [1,17–19]. Magnetic ordering occurs when electron spins correlate into local, often nanoscale, regions of aligned spins. The two most simple classification of magnetic ordering in materials are ferromagnetic ordering where the spins align with one another producing a net local magnetization, and antiferromagnetic ordering where the spins anti-align the bulk net magnetization is close to zero.

Imaging of nanoscale magnetic domains is best accomplished via the contrast mechanism known as x-ray magnetic dichroism (XMD). Dichroism is the difference of how light is absorbed by a material with different polarization of the light. XMD is dependent on the electric field polarization and photon energy of the light [1]. For the strongest XMD contrast, having the photons resonant with a magnetic atomic transition in the sample is critical. For EUV photons, magnetic material will absorb certain polarized photons resonantly at these magnetic transitions (such as the M-edges of iron and cobalt) depending on the orientation of the spin of the magnetic domains and the polarization of the photons [1]. There are two methods of magnetic dichroism: x-ray magnetic circular dichroism (XMCD) - which is more sensitive to ferromagnetic ordering and in the absence of ferromagnetism, x-ray magnetic linear dichroism (XMLD) - which is more sensitive to antiferromagnetic ordering [1](see figure 1.1). Therefore, the ideal source to probe magnetic correlations as well as dynamics of magnetic fluctuations would be a tunable, bright, ultrafast EUV and soft x-ray source with full polarization control.

High harmonic generation of ultrafast laser pulses produces coherent, tunable EUV beams that could be very useful for studying nanomaterials [7, 20–22]. Indeed, HHG has been shown to

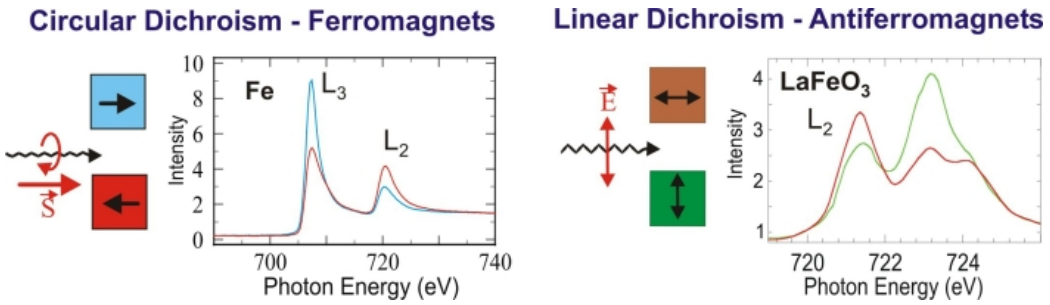

Figure 1.1 Dichroism effects of ferromagnetic and antiferromagnetic materials. Left plot shows circular dichroism effects of ferromagnet, iron. Right plot shows linear dicroism effect of antiferromagnet, perovskite oxide. Taken from [1].

produce high resolution (10-50 nm) images of a variety of samples, including biological samples, thermal dynamics in nanostructures, and even of magnetic domains [23–31]. However, traditionally it was believed that HHG would only be able to produce linearly polarized EUV light bright enough for applications. However, recent work has shown it is possible to produce EUV light with full polarization control from a two color HHG system [10, 11, 31, 32].

EUV photon's short wavelength is useful for obtaining high resolution images and for their elemental sensitivity. The resolution with these wavelengths range between 10 to 50 nm [26, 27]. The EUV range includes several absorption edges (mostly M edges) for many materials, such as iron and cobalt [13]. Therefore, they need to propagate in a vacuum to prevent premature absorption. Depending on their polarization, EUV photons are able to penetrate through very thin layers (about 100 nm for iron) of magnetic material [12]. The transmitted EUV light will diffract as the beam propagates through a thin magnetic sample.

This thesis presents the theory of HHG and how to optimize the signal through phase matching in chapter 2. Chapter 3 will discuss the basics of coherent diffraction imaging using polarized light and how it can be applied for magnetic imaging of magnetic nanosystems, such as magnetic domains in thin ferromagnetic films or superparamagnetic nanoparticles. The tabletop design is explained in detail in chapter 4. The design includes two harmonic selection apparatuses as well as

the MAZEL-TOV device. The MAZEL-TOV is used to generate circularly polarized EUV light for probing ferromagnetic materials. Chapter 5 will present phase matching procedure for optimizing the 42 and 52 eV harmonics. This will be followed by how to set up the MAZEL-TOV including control over the polarization of the fundamental beams. Finally, a demonstration of using the EUV source to reconstruct scatter EUV light from a test diffracting sample.

Chapter 2

High Harmonic Generation

The tabletop source we developed uses HHG. HHG has been well studied and developed over the years [21, 22, 33–36]. It is an extreme non-linear optics process for generating high-energy photons in the EUV and soft x-ray regime by focusing intense, femtosecond (fsec) pulses into dilute gases. The neutral atoms are driven to the point of creating a plasma. At this point, neutral atoms will generate high harmonics. This process will generate a comb of harmonics as depicted in Figure 2.1A. The high harmonics that have been generated are in the EUV and soft x-ray regime(from 10 eV to several keV) [13]. The energy of each harmonic is determined by equation 2.1 where q is the harmonic number, $\hbar$ is Planck's constant, and ω_{IR} is the frequency of the driving laser beam. I will describe HHG with the semi-classical three-step model: 1) ionization of electron, 2) acceleration of electron, and 3) recombination of electron with the parent atom (see Figure 2.1B) [2].

$$E_q = q\hbar\omega_{IR} \tag{2.1}$$

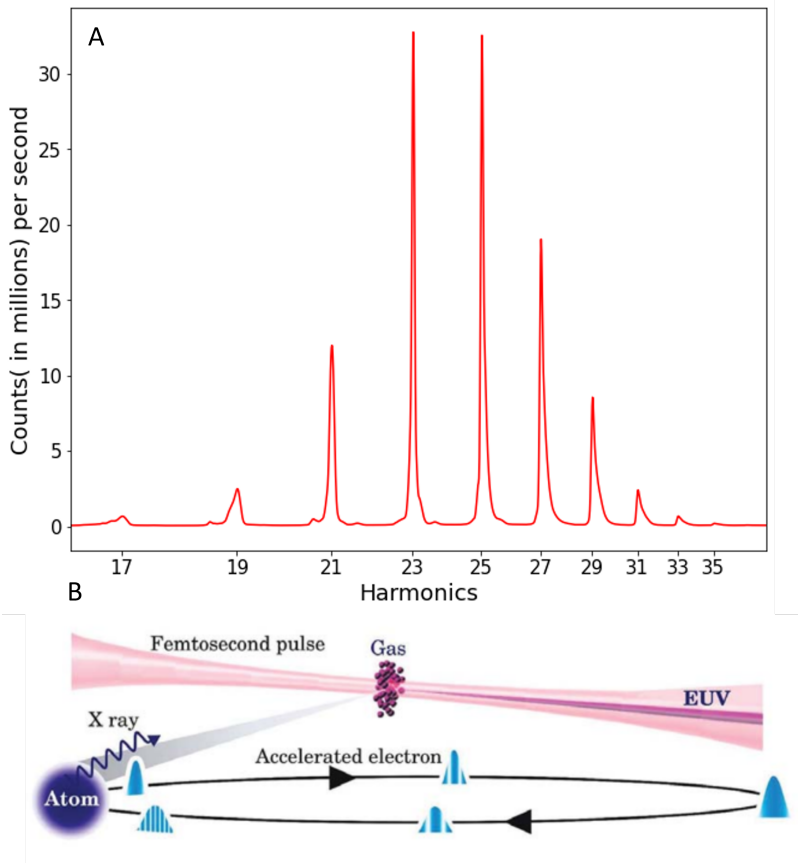

Figure 2.1 (A) High harmonic spectrum measured on our system with an EUV sensitive CCD camera. Only odd harmonics are generated with a monochromatic beam. The harmonics are integer multiples of the IR photon energy (1.55 eV). (B) Diagram of the semi-classical three-step model of the HHG process to produce EUV photons [2]. The process involves the ionization of the electron from the parent atom, acceleration of the electron in the electric field of driving laser, and recombination of the electron with the parent atom generating an EUV photon. (B) was taken from [3].

2.1 Step 1: Ionization of the Electron

The first step in the semi-classical three-step model of HHG is the ionization of the electron. The intense, ultrashort laser pulse produces a strong electric field that distorts the Coulomb potential of a bound valence electron in a gas atom (usually a noble gas). When the Coulomb potential experiences an electric field, it becomes distorted which allows the electron to tunnel out of the potential [37]. If the barrier is suppressed enough, the electron can overcome the barrier. With a

strong enough electric field, the electron is freed from the parent atom and begins to accelerate in the laser's electric field along a certain path. Ionization rates are used when a large number of atoms are considered [2].

2.2 Step 2: Acceleration of Free Electron in the External Electric Field

The second step in the semi-classical three-step model of HHG describes how the free electron gains kinetic energy preparatory to generating a high-energy photon. The electron accelerates as it travels in the laser's electric field. Traditionally, the electric field of the driving laser beam is oscillating and linearly polarized (see Figure 2.2). The free electron's path is dependant on the strength and polarization of the electric field as it travels. If the electric field is linearly polarized, the electron will experience a force that reverses direction which causes the electron to slow down and accelerate back towards the parent atom. The path of the electron depends on the phase of the electric field when it tunnels free from the parent atom [2, 7, 13]. The path determines the velocity of the electron when it returns to the parent atom. The kinetic energy of the electron can be converted into high harmonics when it recombines with the parent atom [2, 7, 13].

Corkum describes the path of the electron classically [2, 13]. The equations of motion of the electron through linear polarized electric field of the laser are given as equations 2.2 - 2.4. When using a monochromatic beam, the electron can only return to the parent atom if the laser beam is linearly polarized [2, 38, 39]. Because the electron is oscillating in a linear motion as given by these equations, the generated high harmonic EUV photons are typically linearly polarized for a monochromatic driving laser beam.

$$x(t) = -\frac{eE_0}{m_e\omega^2}cos(\omega t) + v_0 t + x_0 \tag{2.2}$$

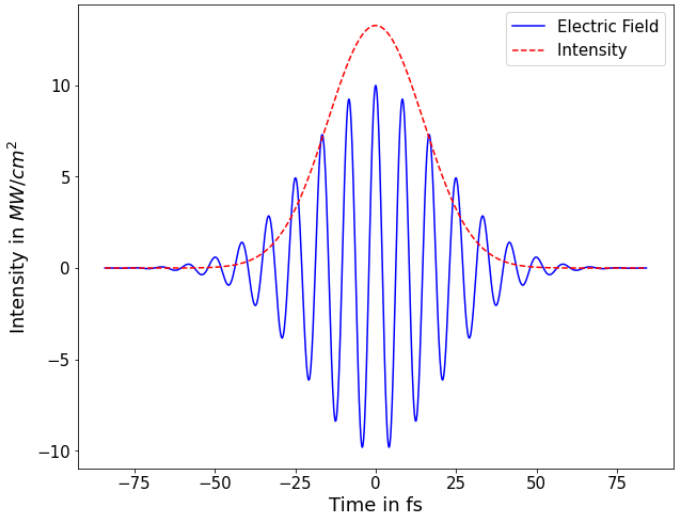

Figure 2.2 Electric field (blue) of a 35 fsec laser pulse. It is oscillating thus the electrons will round trip back to the parent ion. Intensity (red) is proportional to the square of the electric field, $I \propto |E_0|^2$.

$$v(t) = \frac{eE_0}{m_e\omega} sin(\omega t) + v_0 \tag{2.3}$$

$$a(t) = \frac{eE_0}{m_e} cos(\omega t) \tag{2.4}$$

The initial conditions for the position and velocity of the electron are $x(t_0) = 0$ and $v(t_0) = 0$. With these initial conditions, equations 2.2 - 2.4 can be rewritten in terms of the phase of the electric field as equations 2.5 - 2.7 where $\phi = \omega t$ and $\phi_0 = \omega t_0$ [13]. ϕ_0 is the initial phase of the electric field where the electron breaks from the parent ion.

$$x(\phi) = \frac{eE_0}{m_e\omega^2}[cos(\phi_0) - cos(\phi) + (\phi_0 - \phi)sin(\phi_0)] \tag{2.5}$$

$$v(\phi) = \frac{eE_0}{m_e\omega}[sin(\phi) - sin(\phi_0)] \tag{2.6}$$

$$a(\phi) = \frac{eE_0}{m_e} cos(\phi) \tag{2.7}$$

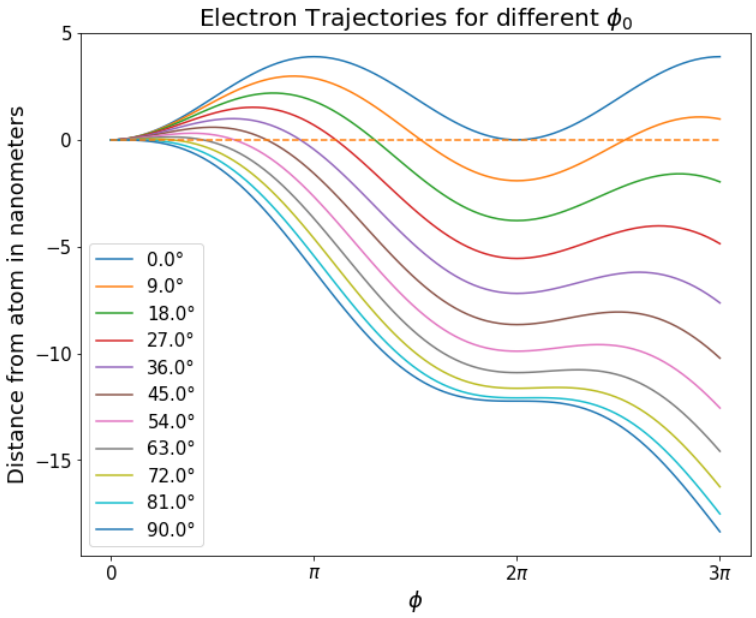

Figure 2.3 Motion of a free electron as it travels in an external electric field of the laser. Each line represents the phase of the laser's electric field where the electron is ionized. The dashed line represents the position of the atom. The laser field phase of 18°corresponds to the trajectory where the electron approaches the parent ion with the maximum kinetic energy. Note that for some initial phase positions, the electron trajectory never returns to the position of the ion.

Figure 2.3 depicts the different paths the electron may travel. The kinetic energy the electron obtains just before it recombines with the parent ion is given in equation 2.8 where U_p is the pondermotive energy. The kinetic energy (Equation 2.8) depends on the initial phase, ϕ_0, and phase ,ϕ, of the electric field. The pondermotive energy is the cycle-averaged energy of a free electron in an electromagnetic field that has no drift component to its motion. It is given as $U_p = \frac{e^2 E_0^2}{4 m_e \omega^2}$ where e is the electron charge, E_0 is the magnitude of the electric field, m_e is the electron mass, and ω is the frequency of the driving laser pulse.

$$T = \frac{1}{2} m_e v^2(t) = 2U_p[sin(\phi) - sin(\phi_0)]^2 \tag{2.8}$$

2.3 Step 3: Recombination of Electron with Parent Ion

The final step of the semi-classical three-step model is recombination of the electron with the parent ion to generate the high-energy photon. As the electron recombines with the parent atom, it will lose the obtained kinetic energy and emit a photon. The energy of the emitted photon is determined by the electron's kinetic energy and the ionization potential atom, $\hbar\omega = \bar{T} + I_p$ [39]. Equation 2.9 is the maximum given energy which occurs when $\phi_0 = 18^o$. Figure 2.4 shows the return energies for various initial phases with the identified maximum at 18^o.

$$\hbar\omega_{max} = 3.17U_p + I_p \tag{2.9}$$

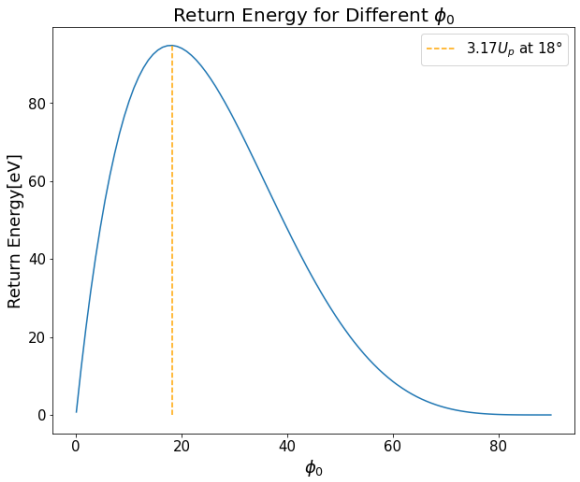

Figure 2.4 Return energies for different initial phases. The maximum has a value of $3.17U_p$ which is where the highest harmonics are generated. This corresponds to an initial phase of 18°.

Our driving laser at BYU produces 800 nm central wavelength pulses with a pulse duration of 35 fsec and 7 mJ per pulse. It is focused down to a 50 micron beam waist into the noble gas. The

maximum photon energy generated with this laser is 322 eV which is in the soft x-ray regime. This concludes the three-step model of harmonic generation of coherent EUV photons.

As we can see in equation 2.9, we need a gas medium with a high ionization potential to produce high-energy photons. This is not only true because of the effect of ionization potential, I_p, in equation 2.9, but also because a higher ionization potential means the electron remains bound later in the pulse when the field is higher, thus increasing U_p. Too low of ionization potential means the electron is liberated at a lower field with a lower pondermotive energy The noble gases are ideal for this process because they have high I_p and also because they are non-reactive. Also, as compared to solid targets, gas targets are self repairing. We have chosen argon gas because of its high ionization potential and it produces a brighter 52.7 eV beam compared to the other noble gases (see Figure 2.5) [4, 33].

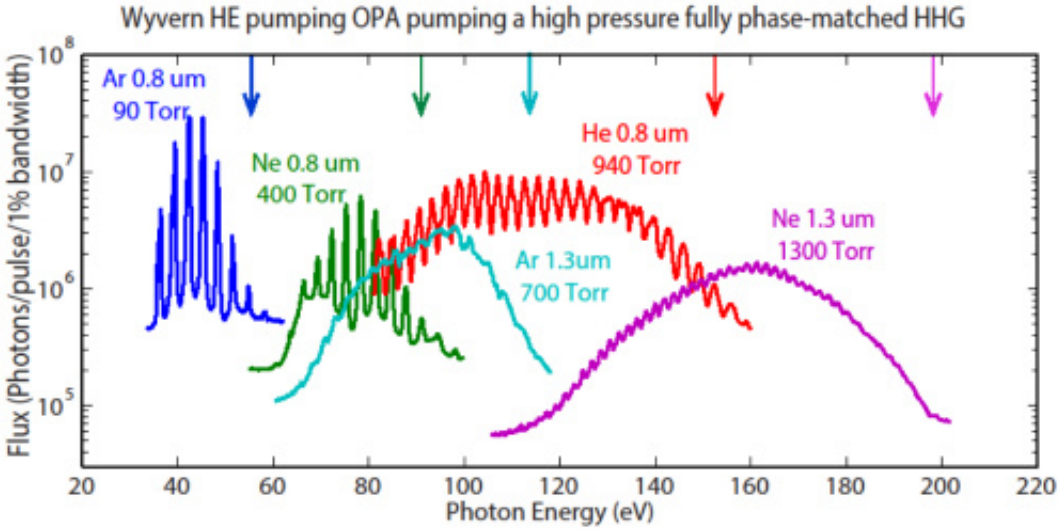

Figure 2.5 Observed harmonics spectra for several nobles gases and wavelengths of driving laser. Taken from [4].

The EUV beam produced by HHG will be used as a source for magnetic imaging. While the previous discussion is from the view point of a single atom, in practice we must consider the ensemble emission characteristics of many atoms. Each atom in a gas is at a different location

and potentially emitting from different phases in the driving laser's electric field. Therefore, we must consider the effects of the combined emitted EUV field [38]. In order to understand this macroscopic emission, we must consider the nonlinear effect of the phase mismatch as discussed in the next section.

2.4 Phase Matching

A reoccurring challenge in nonlinear optics is the phase mismatch between a fundamental electric field and the produced harmonics. The fundamental and generated harmonics experience a difference velocity as they propagate through the gas medium. This velocity difference causes a phase mismatch between the beams which lead to destructive interference. Several factors can contribute to or correct this phase mismatch. Tuning the power of the driving laser beam and pressure of the gas can correct the phase mismatch which will optimize EUV signal [7]. The phase mismatch (Δk) is defined as equation 2.10

$$\Delta k = k_q - qk_0. \tag{2.10}$$

where k_0 and k_q are the wave numbers for the fundamental and generated harmonics with q representing the harmonic order.

We can define a length over which harmonic radiation will be produced in phase by considering the coherence length. The coherence length is the distance the generated harmonic propagates before it is out of phase with the fundamental frequency. After this distance, the generated harmonic will convert back into the fundamental beam. The coherence length is given by equation 2.11.

$$L_{coh} = \frac{\pi}{\Delta k} \tag{2.11}$$

2.4.1 Types of Phase Mismatch

Phase matching involves tuning experimental parameters to make the phase mismatch approach zero which would allow for a large coherence length for the generated harmonic. The processes affecting phase mismatch to be considered are the Gouy phase shift, dispersion due to neutral atoms, and dispersion due to the laser induced plasma. We will discuss these next.

Gouy Phase Mismatch

The Guoy phase mismatch comes a phase variation associated with any beam that goes through a focus. The phase before the focus is shifted by π after the focus. The Gouy phase mismatch is given as equation 2.12

$$\Delta k_{Guoy} = \frac{q}{z_0 + z^2/z_0} \tag{2.12}$$

where q is the harmonic order, z is the distance from the focus, and z_0 is the Rayleigh range [35].The Guoy phase mismatch is minimal when the Rayleigh range is large compared to the harmonic order. Another method to correct this mismatch is to adjust the position of the focus in relation to the medium length such as putting the focus just before or after the gas medium [21].

Dispersion from Neutral Gas

In HHG experiments, noble gases are often used as a target medium. Gases have an index of refraction that approach unity for a very broad range of frequencies. For EUV and x-ray wavelengths, the index of refraction is written as $n(\omega) = 1 - \delta(\omega)$ [13]. The neutral atoms cause a dispersion to both the fundamental driving laser field and generated harmonics, but to different amounts. The dispersion can be rewritten in terms of the index of refraction, $k(\omega) = n(\omega)\frac{\omega}{c}$, as equation 2.13.

$$\Delta k = \frac{2\pi q}{\lambda_0}(n(q\omega) - n(\omega)) \tag{2.13}$$

The real or dispersive part of the index of refraction ($\delta(\omega)$) is very small (about 10^{-5}) . The index scales linearly with pressure and ionization fraction [21, 22, 37]. The ionization fraction determines the number of atoms that are ionized from the IR laser beam. The ionization fraction is defined as $\eta(t) = w_{dc}[E(t)]dt$ where w_{dc} is the ionization rate defined in [2, 37] and $E(t)$ is the magnitude of the electric field. The phase mismatch from the neutral atoms is then written as equation 2.14 where P is the pressure of the gas, P_0 is the standard atmospheric pressure of the gas, and η is the ionization fraction.

$$\Delta k_N = -\frac{2\pi q}{\lambda_0}\frac{P}{P_0}[\delta(q\omega_0) - \delta(\omega_0)](1-\eta) \tag{2.14}$$

Plasma Dispersion

The plasma of free electrons has a different index of refraction from the neutral atoms, and therefore a separate phase mismatch effect. The phase mismatch from the plasma dispersion is given by equation 2.15 [21, 22].

$$\Delta k_{Pl} = \eta N_a r_e \lambda_0 \frac{P}{P_0}\frac{q^2-1}{q} \tag{2.15}$$

where r_e is the classical electron radius and N_a is the density of argon atoms at standard atmospheric pressure.

Phase matching controls the conversion efficiency from the fundamental to the q^{th} harmonic. Each phase mismatch from the focusing geometry, neutral atoms, and free electron are added together as a total phase mismatch. The coherence length approaches large distances as the phase mismatch approaches minimum [21, 22, 34, 35].

Even if perfect phase matching were to be obtained, it would be limited by absorption. Absorption of the gas target has an effect on the produced flux; therefore, the absorption of the argon gas also needs to be considered. The absorption length, equation 2.16, is determined by atomic density,

n_a, and absorption cross-section, σ_{abs} [13, 21, 34]. The harmonics can only propagate for a certain distance in argon before they are absorbed.

$$L_{abs} = \frac{1}{n_a \sigma_{abs}} \tag{2.16}$$

The number of photons generated is optimized according to the following conditions: $L_{med} > 3L_{abs}$ and $L_{coh} > 5L_{abs}$ where L_{med} is the medium length. [34, 35].

2.5 Coherence of High Harmonics

One of the useful aspects of EUV light from HHG is the high degree of coherence [3, 13]. Coherence for a electromagnetic wave means it is well defined and predictable over space and time. If a laser beam is separated and then recombined in an interferometer, if would produce fringe patterns which would only be possible if the laser beam was coherent. An incoherent source would cause the fringe patterns to be washed out [40]. A coherent laser beam is necessary to properly predict how the laser propagates (e.g. diffraction). There are two types of coherence to consider for electromagnetic waves: spatial coherence and temporal coherence. We will discuss each aspect of these types of coherence in the next sections.

2.5.1 Spatial Coherence

Spatial coherence is defined as the predictability of the transverse part of the electromagnetic wave. The coherence length is related to the size of the source and the diverging angle of the electromagnetic wave. Spherical and plane waves are an examples of a electromagnetic sources that have a high degree of spatial coherence. HHG has been shown to generate highly spatially coherent beams [3, 5, 7, 41]. Figure 2.6 shows the results from [5] for determining the spatial coherence of the EUV light generated from high harmonics.

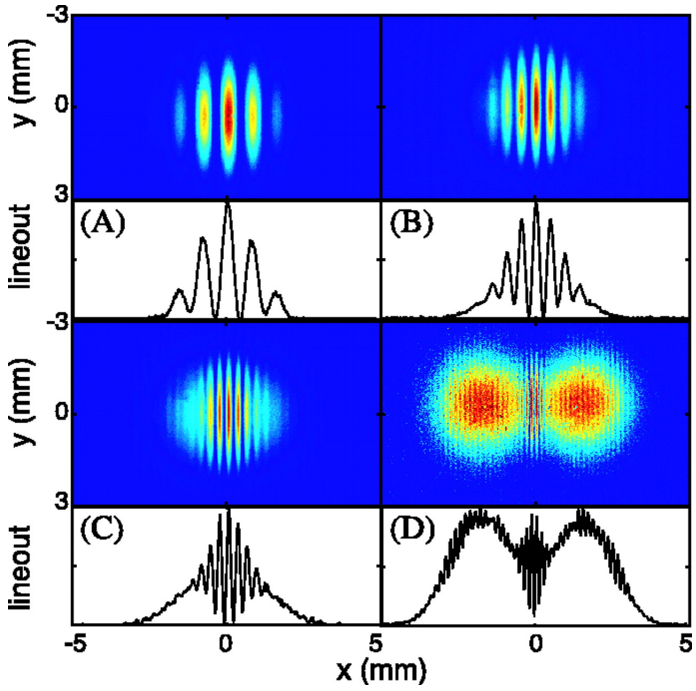

Figure 2.6 Measurements of the spatial coherence of the generated EUV light using two pinhole diffraction. Different pinhole separations were used to obtain each image. The fringe visibility is very high which indicates that HHG produces highly spatially coherent EUV beams. Taken from [5].

Full spatial coherence satisfies equation 2.17

$$d \cdot 2\theta = \lambda / 2\pi \tag{2.17}$$

where d is the source diameter, θ is the divergence half angle, and λ is the wavelength of the light.

2.5.2 Temporal Coherence

Temporal coherence is the tendency for a beam to be predictable over time or wavelength [40]. It is determined by the central wavelength and the bandwidth, $\Delta\lambda$, of the light. An ideal temporally coherent beam has a narrow bandwidth. Equation 2.18 defines the coherence length, l_{coh} that the light must travel before destructive interference proceeds.

$$l_{coh} = \frac{\lambda^2}{2\Delta\lambda} \tag{2.18}$$

A high temporal coherence of the EUV light from HHG has been measured several times [5,42]. The wavelengths of EUV light range from 5 to 40 nm. A characteristic feature HHG is the generation of attosecond pulses. At these wavelengths, the bandwidth is fairly small [13]. This would indicate that HHG generated temporally coherent laser beams.

Chapter 3

Coherent Diffraction Imaging

Having discussed the coherence of HHG, we are now in position to introduce coherent diffraction imaging (CDI). CDI is based on the diffraction of electromagnetic radiation. Diffraction of electromagnetic radiation comes as the beam is incident upon a small object. This can be modeled if the beam is coherent. CDI involves reconstructing diffracted laser beam to obtain an image of the object.

3.1 Theory of Diffraction

I will now briefly review the principles of diffraction of electromagnetic radiation important to understand CDI. The diffraction of light from a sample is described as a two dimensional Fourier transform of the electromagnetic wave immediately behind the sample. Equation 3.1 describes the mathematical formula for the propagation of light from the sample plane to the Fraunhoffer or far-field plane. The derivations can be found in [40, 43].

$$E_{far}(x,y,z) \propto \iint_{sample} \tilde{E}(x',y',0) e^{-i\frac{2\pi}{z\lambda}(xx'+yy')} dx'dy' \tag{3.1}$$

Here E_{far} is the electric field in the far field plane, $\tilde{E}$ is the electric field at the sample's plane, x' and y' are positions on the sample's plane, x and y are positions in the far-field plane, z is the distance between sample and the far-field planes, and λ is the wavelength of the light. Equation 3.1 is a two dimensional Fourier transform between two spatial domains. The electric field $\tilde{E}$ is known as the 'exit surface wave' and is essentially the transmission function of the magnetic domains illuminated by the coherent beam. The modulus squared of E is the diffraction pattern that contains information of the sample. The image of the sample domain can be reconstructed through the use of a iterative two dimensional Fourier transform algorithm. CDI uses these diffraction principles to reconstruct scattered light from a sample. Notice that for diffraction to be predicted from equation 3.1 that the electromagnetic field needs to be coherent. A well defined $\tilde{E}(x',y',0)$, spatial coherence, and a λ, temporal coherence, is necessary to find the diffraction pattern.

By developing a EUV coherent source, we will be able to image polarization sensitive samples such as magnetic domains from a diffraction pattern using CDI. CDI takes advantage of the fact that diffraction is a two dimensional Fourier transform of the transmitted electric field after a sample. The diffracted light carries information about the sample which can be retrieved. One challenge is that detectors only measure the intensity of light. The modulus of the electric field of the diffracted light is related to intensity by the expression $I = |E|^2$. The electric field of light has a phase as shown in the expression $E = E_o e^{i\phi}$. The phase, ϕ, is not measured with the intensity on the detector. Before discussing how to retrieve the phase, I will discuss the important principle of oversampling.

3.2 Oversampling the Diffraction Pattern

What is oversampling and why is it important in CDI? As mentioned above in the discussion on diffraction, there are two planes considered: the sample's plane and the far-field plane. There needs to be sufficient sampling of the diffraction pattern to prevent aliasing. Sufficient sampling is

achieved when one fringe of the diffraction pattern is being measured with at least two pixels on the detector. This is known as oversampling which equation 3.2 describes [7]. Here, z is the distance from detector plane to sample plane, λ is the wavelength of light, D is the sample diameter, p is the pixel width, and OS is oversampling number. Aliasing of the image is prevented if $OS \geq 2$. This could be easily achieved by changing the distance z and the sample or beam size D. We need to apply the principle of oversampling to prevent aliasing of the diffraction pattern and sample.

$$O = \frac{z\lambda}{Dp} \tag{3.2}$$

3.3 Phase Retrieval Algorithms

With the principle of oversampling, we can begin to describe phase retrieval. The missing phase is obtained by iterative phase retrieval algorithms such as those developed by Fienup which include error reduction and hybrid input-output [6]. These algorithms use constraints such as compact support (an assumption that the object is small and compact, or the region where the object must exist is compact), positivity constraint (assumption that the modulus of the amplitude should be positive), and the Fourier constraint (setting the amplitude of the detector siganal wave with the square root of the measured diffraction at each iteration). shrinkwrap is another algorithm which adjusts the compact support and causes it to wrap around the sample leading to a faster converging reconstruction that avoids the twin image problem [44]. An example of the most basic algorithm, known as error reduction, is shown in Figure 3.1 and is described by equations B.1 located in the appendix. The error reduction, hybrid input-output, and shrinkwrap algorithms are often combined and are best used when the sample is smaller than the beam. The compact support constraint cannot be applied if the beam is smaller than the sample. For beams smaller than the sample, a scanning type algorithm such as ptychography will need to be used to reconstruct the sample [45]. These

algorithms are given in appendix B. These are iterative algorithms and they continue until the error reduces to a desired value and the phase converges. With these iterative phase retrieval algorithms, the phase will be retrieved for the electric field for which the image of the sample is obtained. This ends the description of reconstruction algorithms which will be used for imaging polarization sensitive samples such as magnetic domains.

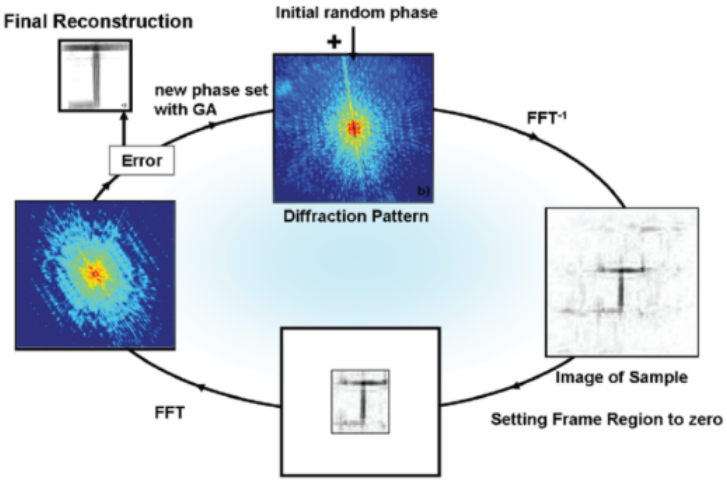

Figure 3.1 Demonstration of the basic principles of iterative phase retrieval knowns as error reduction developed by Fienup [6]. The square root of the measured diffraction pattern in the detector plane is assigned an initial random phase. This is the detector plane that initialises the iterative phase retrieval. This detector wave is then propagated back to the sample plane via an inverse Fourier transform where the compact support constraint is applied. This modified wave is propagated back to the detector plane where an error is computed and the amplitude constraint is applied again, but the phase is allowed to remain. This process continues until the error is reduced and the phases and images converge. Taken from [7].

Chapter 4

EUV Source Design

I will now present the completed design of the tabletop EUV light source. The tabletop source uses the principles of HHG to produce EUV light suitable for CDI of polarization sensitive samples such as magnetic structure in materials. The apparatus is designed for the atomic M-absorption edge of iron at 52.7 eV, the 34^{th} harmonic of the fundamental wavelength of 800 nm from the titanium-dopped sapphire (Ti:sapphire) laser. An important aspect of this design is the ability to have monochromatic EUV laser beam for conducting coherent diffraction imaging as discussed earlier. For other magnetic materials made of several elements, we designed the source to have energy tunability. HHG produces a comb of many harmonics which will require an experimental design that selects the desired harmonic. Here, we will discuss two designs I developed for selection of harmonics: 1) a tunable design consisting of a toroidal mirror and a diffraction grating, 2) a design using normal-incidence multilayered mirrors which reflect a specific harmonic.

The general design of the EUV source for magnetic imaging is depicted in Figure 4.1A. The driving laser is a Ti:sapphire laser focused into an argon gas cell where the high harmonics are generated. The IR beam is blocked by a pair of aluminum filters which are either 0.1 or 0.2 microns thick. The filters attenuate the EUV beam, but about 10% of the the EUV beam passes through the filters [12]. The EUV optics (either the two normal-incidence mirrors or the toroidal mirror

and grating) are used to select the desired harmonic (i.e. monochromatize) and focus the beam onto the sample. The 52.7 eV harmonic is then used to probe a magnetic sample mounted on a three dimensional nanopositioning stage. The diffracted light from the magnetic sample is recorded onto a back-thinned, EUV sensitive charge coupled device (CCD) camera [46]. The apparatus also contains the MAZEL-TOV device which allows full polarization tunability of the harmonics (discussed in section 4.4).

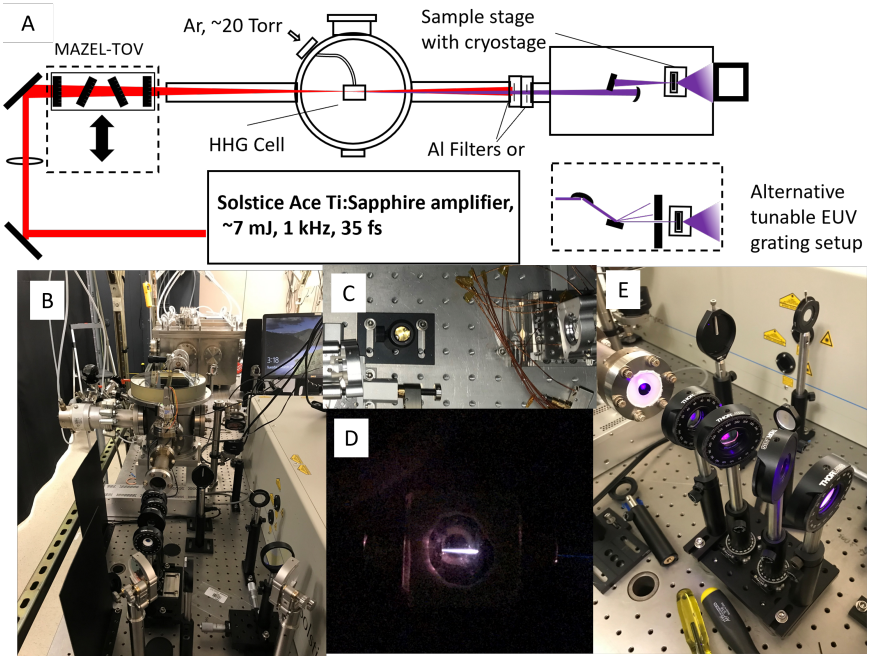

Figure 4.1 (A) Design of the tabletop EUV source for magnetic imaging, consisting of a Solstice Ace Ti:sapphire amplifier, MAZEL-TOV apparatus, a vacuum system, argon gas cell, and two separate optical designs for selecting harmonics.(B) An image of the tabletop source. (C) An image of the EUV normal-incidence mirror design for selecting a harmonic. (D) The IR beam is focused into a gas cell containing argon gas around 20 Torr pressure where the high harmonics are generated. The IR beam is blocked by two aluminum filters placed in series. The EUV beam transfers through the aluminum filters. The desired harmonic is selected either by normal-incidence EUV mirrors or a toroidal mirror and grating pair. The selected harmonic is then used to probe the sample. (E) The system also contains the insertable MAZEL-TOV apparatus. This allows full polarization tunability between linear and circular polarization. It is important to note that the MAZEL-TOV may not work with the tunable spectrometer since the EUV beam will be at grazing incidence for each optic. This can alter the polarization of the beam.

4.1 Tunable Harmonics Design

In this section, I introduce the tunable design I developed which consists the toroidal mirror and diffraction grating optics. I designed and ordered the parts, but began using a grating long-focal-length spherical substrate from the Peatross lab. I have not yet implemented the new optics. This was in part due to long delays due to the COVID-19 pandemic. The diffracted harmonics will propagate to a slit which will only allow one of them through. The harmonic selection is done by tilting the diffraction grating. Each of these optics will be discussed.

4.1.1 Toroidal Mirror

Toroidal mirrors are ideal for reflecting high-energy photons due to their design for grazing incidence. Single element metal mirrors do not reflect high-energy photons at normal-incidence very well. Grazing incidence metal mirrors provide broadband reflectance [13]. Toroidal mirrors have two radii of curvature which are orthogonal to each other as shown in Figure 4.2.

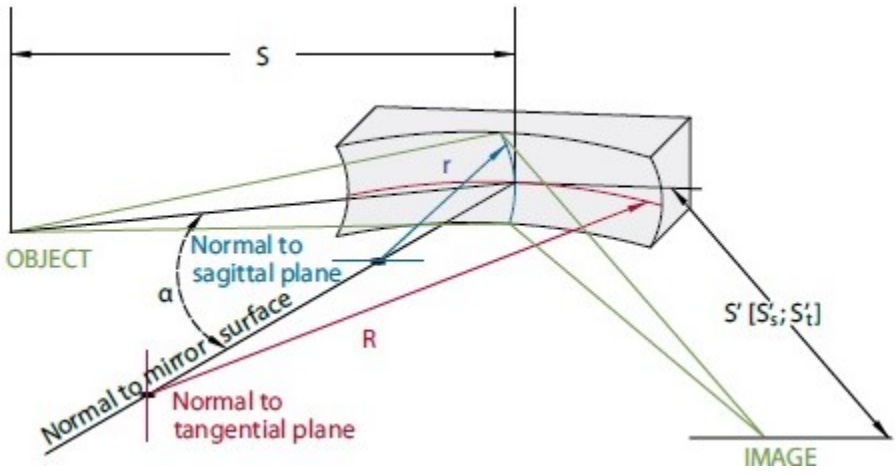

Figure 4.2 Toroidal mirror graphic. It displays the radii of curvature with identified tangential and sagittal planes. Taken from [8].

Toroidal mirrors are designed for grazing incidence reflections and to reduce astigmatism and aberrations that would affect other focusing optics at grazing incidence (for example, a normal-incidence spherical mirror). In optics, there are two orthogonal planes considered for ray tracing known as the sagittal and tangential planes. These planes are considered when using off axis curved mirrors such as toroidal mirrors.

Toroidal mirrors have two variable focal-lengths which depend on the radii and angle of incidence of the beam. Figure 4.2 shows the geometry of a toroidal mirror where r is radius of curvature normal to sagittal plane, R is the radius of curvature normal to the tangential plane, α is the angle of normal-incidence, S is the distance between the object to the toroidal mirror, S_t' is the tangential image point, and S_s' is the sagittal image point. The focal-lengths are given by equations 4.1 and 4.2 where f_t is the focal-length of the tangential plane and f_s is the focal-length of the sagittal plane.

$$\frac{1}{S}+\frac{1}{S_s'}=\frac{1}{f_s}=\frac{2cos(\alpha)}{r} \tag{4.1}$$

$$\frac{1}{S}+\frac{1}{S_t'}=\frac{1}{f_t}=\frac{2}{Rcos(\alpha)} \tag{4.2}$$

There is an angle at which the focal-lengths are the same. Setting the focal-lengths equal to each other and solving for the $cos(\alpha)$ leads to equation 4.3.

$$cos(\alpha_{proper})=\sqrt{\frac{r}{R}} \tag{4.3}$$

Equation 4.3 implies that toroidal mirrors will only focus with a particular angle, α_{proper}, without distorting the image via aberrations (primarily astigmatism). In other words, they only work properly at one angle of incidence. At other angles of incidence, the tangential and sagittal focal-lengths will be different.

I designed three toroidal mirrors for the high harmonic system which were manufactured by ARW Optical [47]. The three mirrors are designed for 10^o grazing incidence and are coated with gold. Gold is a fairly good broadband reflective mirror for EUV wavelengths (e.g. 52.7 eV has a reflectivity of 67% at 10^o [12]). The radii of the three designs are given in Table 4.1.

Design	R	r
1	7230 mm	220 mm
2	3940 mm	120 mm
3	5160 mm	160 mm

Table 4.1 Radii curvatures of the toroidal mirrors from ARW Optical. They are designed to reflect at 10^o grazing incidence to minimize astigmatism. Reflections of the 52.7 eV harmonics from gold surface mirrors will be approximately 67% [12]

.

4.1.2 Diffraction Grating

After the toroidal mirror, the EUV light will be incident on a flat diffraction grating. The flat diffraction grating will separate the harmonics based on their wavelength at a grazing incidence angle. Diffraction from a grating is given in equation 4.4:

$$md\lambda = sin(\beta) + sin(\theta) \tag{4.4}$$

where m is the diffraction order, d is the number of grooves per millimeter of the diffraction grating, λ is the wavelength of the EUV beam, θ is the angle of normal-incidence on the grating, and β is the diffracted angle (see also Figure 4.3). We obtained an EUV flat grating from Richardson Grating. It has 1200 grooves per mm and blazed at 29 nm wavelength or 1^o blaze angle. It is coated with gold and has the dimensions of 50 mm by 50 mm by 10 mm.

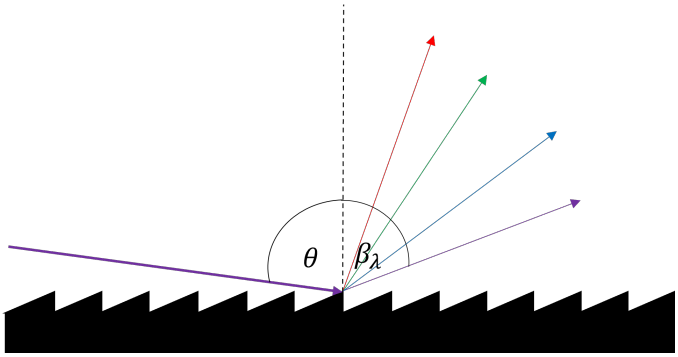

Figure 4.3 Diagram of the function of the diffraction grating. The grating will separate the harmonics into individual beam as described by equation 4.4

.

4.2 Normal-incidence EUV Mirrors Design

The second design for monochromatizing the beam and selecting a single harmonic uses multilayered mirrors designed to reflect specific photon energies at normal-incidence. We purchased superpolished mirror substrates with various radii of curvature from G&H. Reflective EUV multilayer coatings were then designed and coated by Eric Gullikson of the Center for X-ray Optics at Lawrence Berkeley National Laboratory [12]. The mirrors consists of sets of flat and curved mirrors designed for optimal reflection for 42 or 52 eV photons. Reflection curves for the two sets of mirrors are shown in Figure 4.4. Additional reflection curves of the other mirrors can be found in the appendix as Figures C.1 and C.2. The normal-incidence mirrors will not have as high as a reflection compared to the grazing incidence design. A more detailed description of normal-incidence EUV mirrors can be found in David Attwood's book [13].

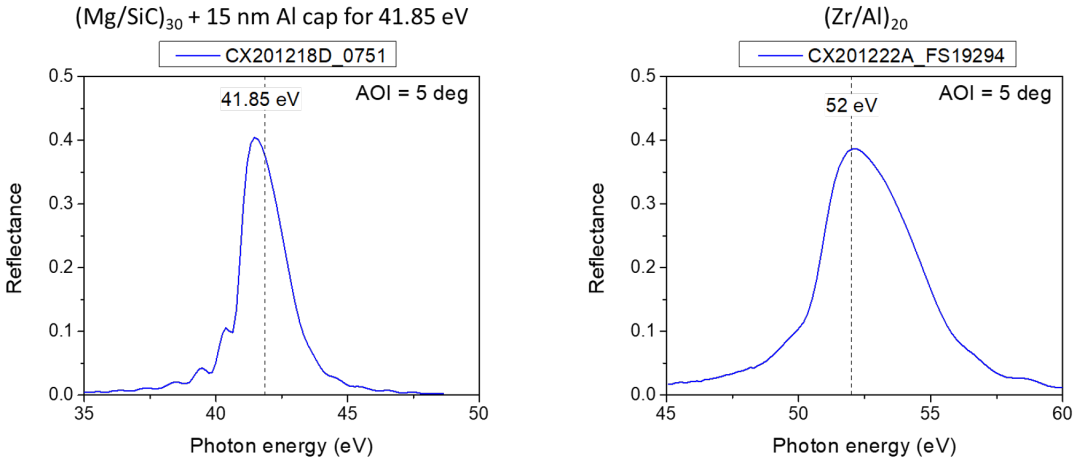

Figure 4.4 Measured reflection curves for the two sets of EUV mirrors. One is designed for 41.85 eV and the other is designed for 52 eV wavelengths. These mirrors are designed to reflect at angle of 5^o normal-incidence.

4.3 Ti:Sapphire Laser

The driving laser for the HHG is an Ace Solstice Ti:Sapphire laser from Spectra-Physics with a max pulse energy of 7 mJ, repetition rate of 1 kHz, and pulse duration as short as 35 fsec. The central wavelength is 800 nm with a 40 nm bandwidth. The laser consists of an Ti:sapphire oscillator which passively mode locks (using the optical Kerr effect [48]) and a chirped pulse amplifier. The laser is capable of tuning the output power and pulse duration. The harmonics are multiples of the IR photon energy 1.55 eV.

4.4 MAZEL-TOV

HHG with a monochromatic beam requires linearly polarized light [2]. For many years, the prevailing theory was that only linearly polarized high harmonics could be generated due to the need of the free electron to return to the parent ion, thus necessitating linearly polarized electric fields. Circular polarization in the driving laser was assumed to make the free electron spin away from the parent ion and not recombine. Generating circularly polarized high harmonics has been demonstrated successfully using a bichromatic (two color) beam [10, 11, 32]. The bichromatic beam consists of left circularly polarized IR and its right circularly polarized second harmonic, or vice versa. The beams combine to form a threefold Spiderwort pattern shown in Figure 4.5. The harmonics generated with this pattern are circularly polarized [10, 11].

The harmonics consist of odd and even harmonics with the suppression of every third harmonic [10, 11, 32, 49, 50]. The suppression of the third harmonic is a consequence of the conservation of energy and spin angular momentum between the interactions of the photons with the argon atoms. Conservation of energy requires that the number of IR ($l\omega_{IR}$) and blue ($n\omega_{blue}$) photons should be equal to the generated harmonic (ω_c) as shown in equation 4.5 where $\hbar$ is Plank's constant.

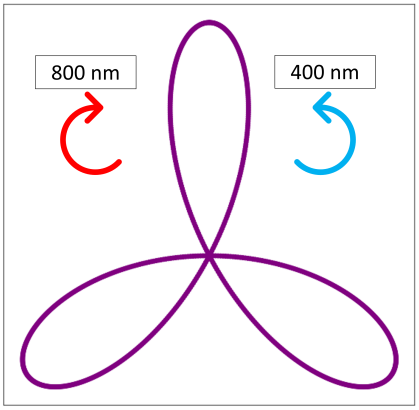

Figure 4.5 Threefold pattern of the electric field polarization formed through the combination of IR (left circular) with its second harmonic (right circular). The IR and blue beams are circularly polarized and have opposite helicities. An electric field with this pattern generates circularly polarized high harmonics.

$$\hbar\omega_c = l\hbar\omega_{IR} + n\hbar\omega_{blue} \tag{4.5}$$

Conservation of spin angular momentum requires the number of IR photons to be one more or less than the blue photons, $l = n \pm 1$ [11, 50]. The allowed generated harmonics are thus $\hbar\omega_c = (3n \pm 1)\hbar\omega$. Figure 4.6 shows a diagram of these conservation laws and how they determine the allowed harmonics.

Kfir *et al* demonstrated a successful generation of circularly polarized harmonics using a Mach-Zeinder interferometer [11, 32]. A few years later, a simpler inline design, called the MAZEL-TOV, was developed by Oren Cohen's group at the Technion University [31]. MAZEL-TOV is an acronym that means MAch-ZEhnder-Less for Threefold Optical Virginia spiderwort.

Figure 4.7 depicts the MAZEL-TOV apparatus. It consists of a BBO crystal, two calcite plates, and an achromatic quarter-wave plate. The MAZEL-TOV is placed after the focusing lens so the IR and second harmonic beam are aligned spatially and focus at the same point. An EUV high harmonic source with the MAZEL-TOV has previously been used to image magnetic domains [31]. In the next sections we will describe the operation of each of the elements of the MAZEL-TOV.

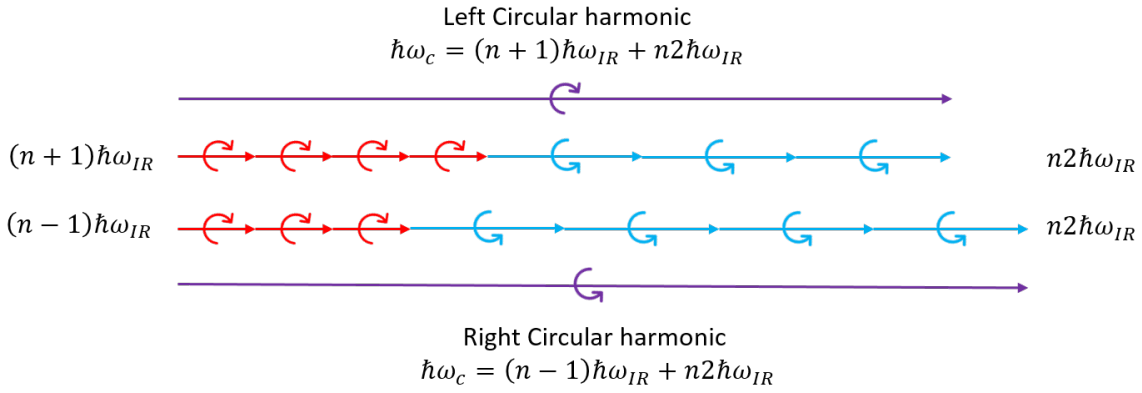

Figure 4.6 Diagram describing how left circularly polarized IR photons combined with right circularly polarized blue photons to generate either a right or left circularly polarized EUV beam. The conservation of energy requires that the generated EUV photon energy is the sum of the number of IR and blue photons energies. Angular momentum conservation requires the difference in number of IR to blue photons to be ± 1.

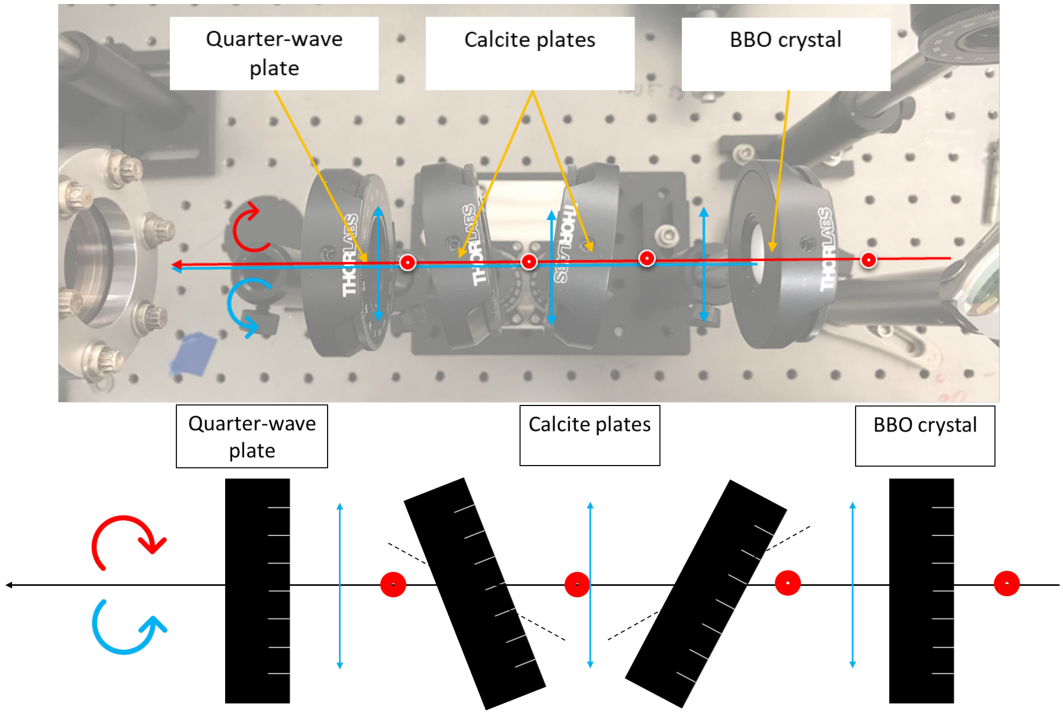

Figure 4.7 Schematic of the MAZEL-TOV apparatus. The o-polarized IR beam is converted to a bichromatic circularly polarized beam which is used to generate circularly polarized high harmonics. Top picture of the MAZEL-TOV apparatus is included.

4.4.1 BBO Crystal

The BBO crystal converts 30% of the o-polarized IR (800 nm) laser beam into the second harmonic e-polarized blue (400 nm) laser beam. In our experiment, the o-polarization corresponds to s polarization while the e-polarization corresponds to the p polarization (see optics book [40] for definitions of s and p polarization). This is type I phase matching for the second harmonic generation. Second harmonic generation is well described in Robert Boyd's *Nonlinear Optics* book [51]. The IR and blue pulses propagate together after the BBO crystal. These pulses experience a group velocity mismatch (GVM) as they propagate through optics downstream from the BBO crystal. The temporal misalignment between the IR and blue pulses will prevent the formation of the threefold Spiderwort pattern described previously (see section 4.4). This must be corrected to generate the circularly polarized high harmonics.

4.4.2 Calcite Plates

The purpose of the calcite plates is to precompensate the IR and blue pulses to correct the GVM [52]. In most materials, IR pulses experience a lower index of refraction compared to the blue pulses. Thus, IR pulses propagate faster than blue pulses through most material. This is the GVM and it is shown as equation 4.6

$$GVM = \frac{1}{v_g(400\ nm)} - \frac{1}{v_g(800\ nm)} \tag{4.6}$$

where $v_g(800\ nm)$ and $v_g(400\ nm)$ are the group velocities for the IR and blue pulses, respectively. For a length d of a material, the time delay τ between the IR and blue pulse is given by $\tau = GVM \times d$. We can expand the first term of equation 4.6 using a Taylor expansion centered about the frequency of 800 nm. This gives an alternative form of the GVM given as equation 4.7

$$GVM = -GVD(\omega_{800\ nm}) \times (\omega_{800\ nm} - \omega_{400\ nm}) \tag{4.7}$$

where GVD is the group velocity dispersion of the IR pulse for a given material and ω_λ are the angular frequencies of the light pulses.

The calcite plates pre-compensate the IR and blue pulses so they align temporally as shown in Figure 4.8. Calcite plates were chosen because of their strong negative birefringence ($n_e - n_o = -0.172$ for IR). This allows an e-polarized beam to experience a smaller index of refraction compared to an o-polarized beam. The o-polarized IR beam and e-polarized blue beam experience ordinary and extraordinary indices of refraction of 1.6488 and 1.4972, respectively [53]. Therefore, the blue pulses propagate with a faster velocity compared to the red pulses in a calcite crystal. The GVM mismatch from the quarter-wave plate and optical window is corrected using these calcite plates. Also, the calcite plates must be anti-reflective coated for both 800 and 400 nm wavelengths.

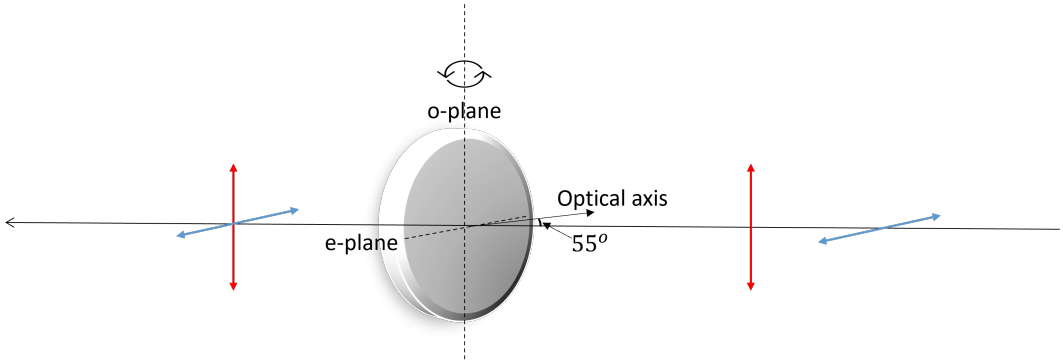

Figure 4.8 Diagram of the functionality of a calcite plate. The group velocity mismatch between the IR and blue pulse is corrected as they pass through the plate. The IR beam is aligned along the ordinary plane of the crystal while the blue beam is aligned along the extraordinary plane. The optical axis makes an angle of 55^o from the normal axis to the surface of the crystal. Tilting the calcite crystal adjusts the extraordinary index of refraction which varies the group velocity of the blue pulse.

The extraordinary index of refraction of the blue beam, $2\omega_{IR}$, is dependent on the polar angle θ that the incident beam makes with the optical axis of the calcite crystal as described by equation

4.8 [40].

$$\frac{1}{n_e^2(\theta)[2\omega_{IR}]} = \frac{cos^2(\theta)}{n_o^2[2\omega_{IR}]} + \frac{sin^2(\theta)}{n_e^2[2\omega_{IR}]} \tag{4.8}$$

Since the extraordinary index of refraction varies by angle of incidence on the plate, the calcite crystal can be tuned change the velocity of the blue pulses as they propagate through the calcite [52]. The MAZEL-TOV uses a pair of calcite plates, with their optical axes pointing towards each other, to prevent walk off beams caused by the birefringence of the crystal.

4.4.3 Quarter-wave Plate and Optical Window

The final optics are the quarter-wave plate and optical window. The achromatic quarter-wave plate orientated at $\pm 45^o$ to the fast axis transforms the linearly polarized IR and blue beams into circularly polarized beams. The window is just the entrance window to the vacuum chamber for the IR and blue beams. We note here that it is very important that the window does not have any birefringence effects. For a while, we had used a sapphire single crystal window which introduced some birefringence and was preventing the generation of circular harmonics. We then switched the window to a UV fused silica window that did not have birefringence effects. Additionally, these optics also should be anti-reflective coated for both 800 and 400 nm wavelengths. With the BBO crystal, calcite plates, and quarter-wave plate aligned, we can form the bichromatic electric field polarization in the form of a threefold Virginia Spiderwort pattern which in turn generates circularly polarized high harmonics with every third harmonic suppressed [10].

Chapter 5

Experimental Set Up and Results of the Tabletop EUV Source

Here we present our results the developed polarization controllable tabletop EUV source. The 42 eV harmonic will be discussed first following by the 52 eV harmonic. Next, the results of the MAZEL-TOV are given . Finally, I used the EUV source to obtain a diffraction pattern from a double pinhole which is then reconstructed into a real space image using iterative phase retrieval.

5.1 Optimization the Harmonics

Generation of coherent harmonics are optimized by phase matching. The dispersion due to the neutral gas, plasma, and the Gouy phase shift is considered for the phase mismatch. The dispersion of the neutral gas and plasma are coupled through the gas pressure and intensity of the IR laser beam. The pressure is controlled with a mass flow controller. The intensity is tuned with several different parameters such as the laser output, pulse duration, focal-length of lens, and the lens position. We took data sets to observe the behavior of the signal as we tune the laser power output and pressure of the argon gas.

The medium length is a parameter that is not adjustable while under vacuum. Therefore, several different medium lengths are used to determine the best harmonic signal. We optimized the 42 eV harmonic for each medium length. A long medium length would allow more atoms to be ionized for the HHG process. Absorption is considered with the medium length. The medium length needs to be short enough to prevent excessive absorption while also long enough to produce maximum signal.

Optimization has been accomplished for the 42 and 52 eV harmonics. Each harmonic was isolated using a set of the corresponding normal-incidence EUV mirrors. The signal is recorded onto the CCD camera as an array of measured counts over time the HHG process occurred. The data was processed with python to obtain the total counts per second and then converted to photons per second. The number of photons per second is found by applying equation 5.1 where N_γ is the number of photons, N_{counts} is the number of counts detected in each pixel of the CCD, K is the gain factor, and E_{gamma} is the energy of photons that the CCD is detecting [54].

$$N_\gamma = N_{counts} K \frac{3.65}{E_\gamma} \tag{5.1}$$

5.1.1 Optimization of the 42 eV Harmonic

We began the study to generate the 42 eV beam, the 27^{th} harmonic. Figure 5.1 shows a three dimensional plot of the number of photon counts per second as a function of laser power output and the pressure of the argon gas. We can see that a 3.36 W laser output and a pressure of 26 Torr has the brightest signal. Figure 5.2 shows a two dimensional version of Figure 5.1. From Figure 5.2 we can see that the pressure tends to favor 26 Torr for all laser power outputs. Figure 5.3 shows the beam profiles for various pressures at laser power output of 3.36 Watts.

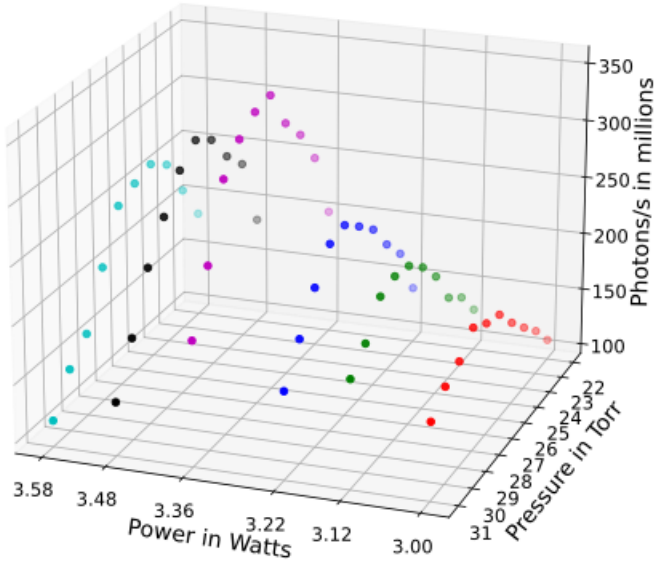

Figure 5.1 Three dimensional plot of 42 eV photon counts per second with dependence on the output power of the laser and pressure of the argon gas. This was done with a medium length of 10 mm and lens of focal-length 1000 mm. The optimal phase matching conditions favor a power of 3.36 Watts with gas pressure of 26 Torr.

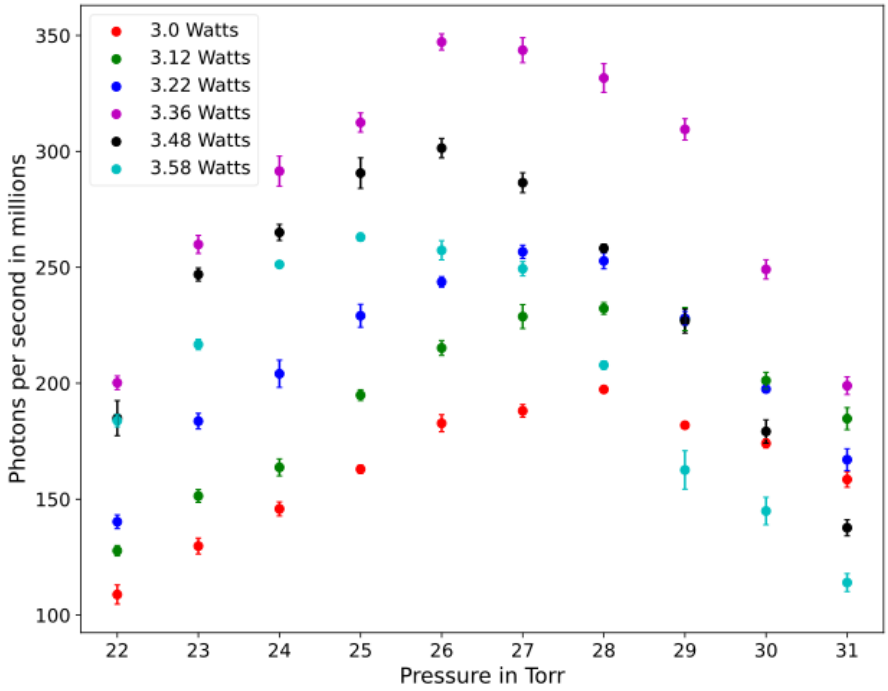

Figure 5.2 Two dimensional plot of the pressure power study. This shows that the phase matching tends to favor from 26 to 28 Torr for different powers.

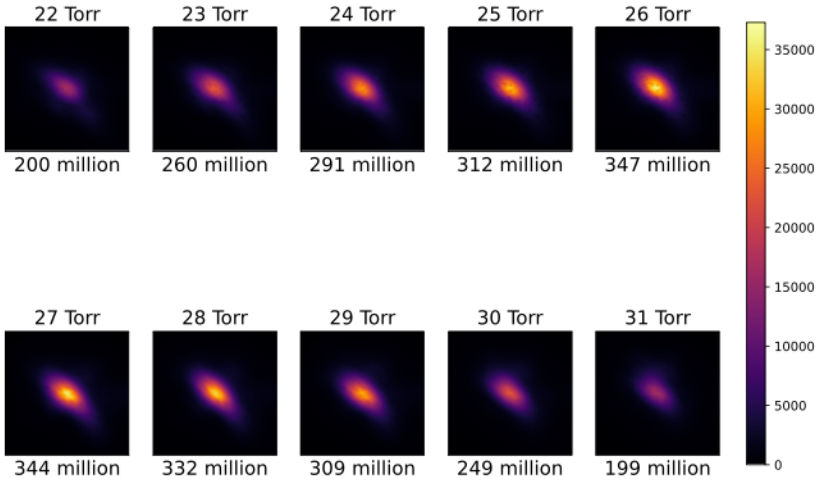

Figure 5.3 Beam profiles at different pressures with power set at 3.36 Watts. We used a 10 mm medium length and 1000 mm focal-length lens. The images were scaled to the maximum value in the 26 Torr image. Each image reports the pressure and the number of photons per second detected on the CCD camera.

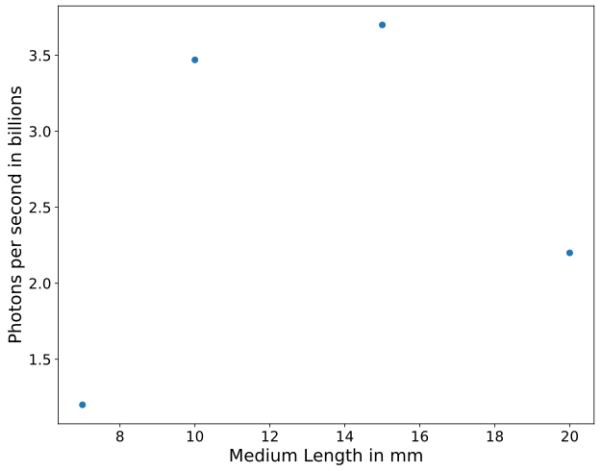

Figure 5.4 Plot of the number of photons per second for different medium lengths. The plot shows a 15 mm medium length is optimal for 42 eV harmonics. This data was obtain while using a 1500 mm lens.

Figure 5.4 shows the results of how the medium length affects the optimization of the 42 eV harmonic. The optimal medium length was 15 mm. A 1500 mm focal-length lens was used when taking the data for Figure 5.4. The signal was weaker when a 20 mm medium length was used; thus, this indicates excessive absorption. The optimal laser power output and pressure of the gas was not consistent for each medium length. For a given medium length, the optimal power and pressure was different.

After several weeks of optimization, we have been able to achieve highly phase matched conditions for the 42 eV harmonic. A medium length of 15 mm was used with a pressure of 12 Torr and laser power output of 1.53 Watts. The IR beam was blocked with two 0.2 micron aluminum filters. The measured value was about 1.5 billion photons per second. Figure 5.5 shows the beam profile of the best signal for the 42 eV harmonic.

I have measured the transmission difference between the 0.1 and 0.2 micron aluminum filters. The transmission difference between the aluminum filters of the 42 and 52 eV harmonics were completed and the results are in appendix D. The transmission different between the 0.2 micron and the 0.1 micron filters is about 19% (see Table D.1 in appendix). Using the 19% transmission

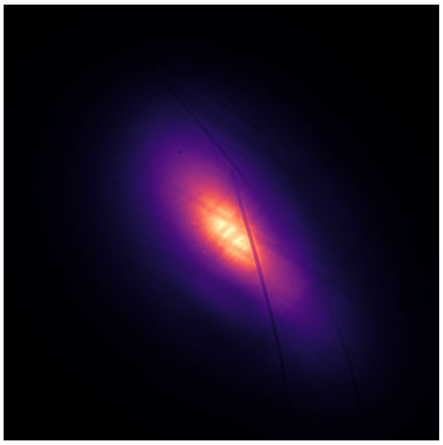

Figure 5.5 Beam profile of the optimized 42 eV beam. A medium length of 15 mm with a lens focal-length of 1500 mm was used with this data set. The number of photon counts is 1.5 billion photons per second. Two 0.2 micron aluminum filters were used to take this data. If 0.1 micron filters are used instead, the total photons would be approximately 8.1 billion per second.

difference, I calculated that the 42 eV harmonic to have about 8.1 billion photons per second incident onto the CCD camera. This is if two 0.2 micron aluminum filters were replaced with the 0.1 micron aluminum filters.

5.1.2 Optimization of the 52 eV Harmonics

The next harmonic we optimized was the 52 eV harmonic. This harmonic is near resonance with the iron edge [13]. These harmonics required both higher intensities and pressure. After several weeks of optimization, I have been able to achieve a bright source of about 283 million photons per second. Two 0.2 micron aluminum filters were used. If two 0.1 aluminum filters were used the number of photons per second incident on the CCD camera would have been 1.5 billion photons per second (see Table D.2 for transmission conversions for 52 eV). A laser output of 3.29 Watts with a 1500 mm lens and a pressure of 14.9 Torr were the parameters of this signal. Figure 5.6 shows the beam profile of this harmonic measured on the CCD camera. Unfortunately, 3.29 Watts with a 1500 mm lens would cause our aluminum filters to be burned.

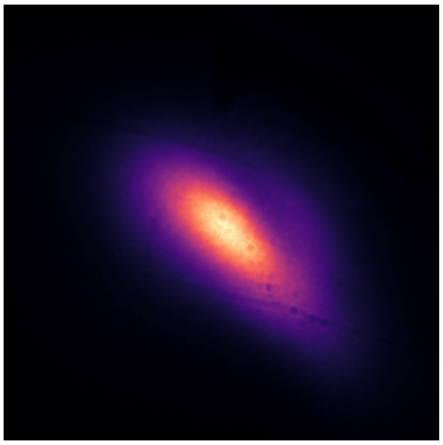

Figure 5.6 Beam profile of the 52 eV harmonic. A medium length of 20 mm with a lens focal-length of 1500 mm was used with this data set. The measured value was 283 million photons per second. Two 0.2 micron aluminum filters were used to take this data. If 0.1 micron filters are used instead the total photons would be approximately 1.5 billion per second.

We exchanged the 1500 mm lens with a 1000 mm lens and then proceeded with the 52 eV harmonic. We wanted to find parameters for which the filters would be able to survive. The best parameters found are laser output of 3.6 Watts, a medium length of 7 mm, and pressure of 27 Torr with argon gas. The filters can survive 3.6 Watts if a 1000 mm lens is used. Figure 5.7 shows the beam profile using these parameters. The number of photons per second was 581 million. However, these parameters do not produce the best phase matching conditions. The optimal signal of the generation of 52 eV harmonic was 848 million photons per second. However, the power required was 5.62 Watts which would burn the filters. Comparing the 1000 mm focal-length lens data to the 1500 mm lens data shows that the signal was weaker for a shorter focal-length lens.

I have demonstrated that we can generate both 42 and 52 eV harmonics. We now have a source that can produce a bright 52 eV beam for probing iron samples at the iron M-absorption edge. More optimization can be done for other harmonics to obtain a more complete data set for all the harmonics needed for polarization sensitive imaging such as magnetic imaging.

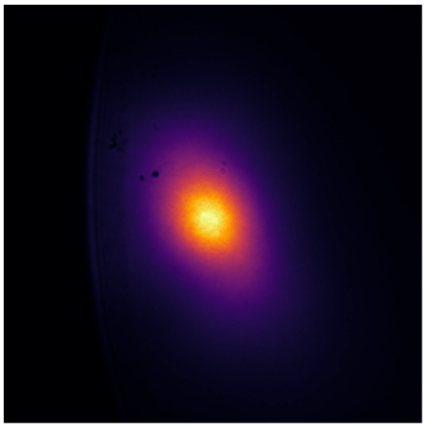

Figure 5.7 Beam profile of 52 eV harmonic that will be used for experiments in magnetic imaging. The parameters were 3.6 Watts with a 1000 mm lens, 7 mm medium length, and 27 Torr gas pressure. The number of photons per second measured onto the CCD detector was 581 million.

5.2 Results for MAZEL-TOV

The MAZEL-TOV required careful alignment of the birefringent optics in order to control the polarization. We ordered each of the optics from Eksma optics. The BBO crystal is cut for type I phase matching ($\theta = 29.2^o$, $\phi = 90^o$) and has dimensions of 10 mm x 10 mm x 1 mm. The polarization of the IR beam was o-polarized before entering into the BBO crystal for maximum conversion from the IR laser beam to blue laser beam. The BBO converts two o-polarized IR photons into one e-polarized blue photon. We then adjust the pulse delay between the IR and blue pulses with the calcite plates.

The calcite plates purpose is to precompensate the pulse delay between the IR and blue pulse so they align temporally after they propagate through the quarter-wave plate and optical window. The plates are 16 x 14 mm crystals designed for $\pm 10^o$ angle of normal-incidence. This corresponds to a compensation range of 370 to 520 fsec for each calcite plate (see Figure 5.8).

The optical axis of a calcite plate is 55^o normal to the surface. The calcite plates are oriented such that the optical axis is parallel to the polarization of the blue beam. The optical axes for both

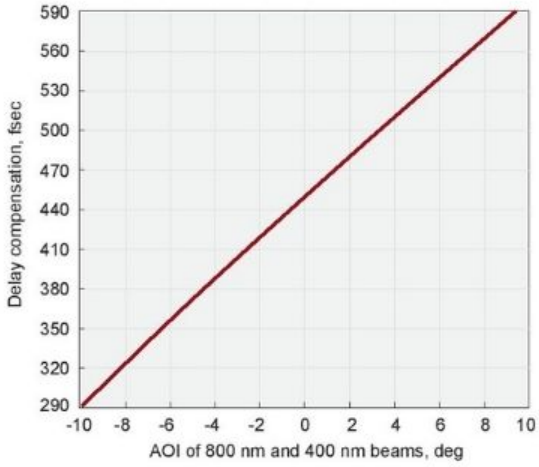

Figure 5.8 Plot of group delay compensation versus angle of incidence of one calcite plate. The plot is fitted to an equation of a line, $Delay = 16\frac{fsec}{degree}AOI + 450fsec$. Taken from Ekmsa Optics [9].

calcite plates needs to be pointing inwardly. This ensures there is no walk off beam and for the angle between the beam and the optical axis to be the same for both plates. I calculated the pulse delay for the sapphire window (1 mm) and the quarter-wave plate (0.6 mm) to be about 400 fsec which corresponds to an angle incidence of about 15^o for both calcite plates. With IR and blue pulses precompensated, they would temporally aligned after the optical window. We replaced the sapphire window with a 3 mm fused silica window for reasons discussed in chapter 4. The GVM for the quarter-wave plate and 3 mm fused silica window is about 640 fsec. After successful alignment, the measured angle of incidence is used to determine the actual pulse delay from Figure 5.8.

The quarter-wave plate converts the o-polarized IR and e-polarized blue beams into circularly polarized beams with each beam having the opposite helicity. This ensures we have a combined electric field of a threefold Spiderwort pattern.

The circularly polarized EUV beam is analyzed with spectrometer consisting of a flat silver mirror and spherical grating. The EUV beam was at grazing incidence of 17^o and 14^o for the silver

mirror and grating, respectively. The calcite plates were tilted until we saw harmonic pairs which indicate that we have circularly polarized EUV light [10]. The diffraction grating was loaned to us by Dr. Justin Peatross. The grating has 1200 grooves per mm and a radius of curvature of 2 m. The toroidal mirrors were designed to be used with a flat grating. Because of this, it was necessary to replace the toroidal mirror with a flat silver mirror.

Alignment of the MAZEL-TOV was successful. A challenge of alignment involved controlling the polarization the bichromatic beam. Every optic involved with the MAZEL-TOV are birefringent which can significantly alter the polarization of the bichromatic beam. The BBO crystal and the calcite plates must be oriented such that the principal axes of the crystals are aligned with the polarization of the bichromatic beam. One of the ordinary axes need to be aligned with the IR polarization. The other ordinary and the extraordinary axis required to be aligned with the polarization of the blue beam. A dichroic mirror with two linear polarizers were used to analyze the polarization of both the IR and blue beams. We observed odd and even harmonics with the sapphire window inserted. However, tilting the calcite plates did not produce harmonic pairs due to polarization scrambling of the bichromatic beam due to the birefringence of the sapphire window. The sapphire window was replaced with a 3 mm fused silica window. Fused silica does not have any birefringence unlike the sapphire window. Tilting the calcite plates with the new window produced harmonic pairs. With the fused silica window inserted, I have managed to recreate the signal observed through the sapphire window. The quarter-wave plate was oriented at an angle that would turn the polarization to elliptically polarized with ellipticity less than one. This showed odd and even harmonics with no harmonic pairs. This implies that the harmonics observed through the sapphire window could be elliptically polarized [55].

My results of the MAZEL-TOV are shown in Figure 5.9. Figure 5.9 (A) is the image of the spectrum of the generated circularly polarized high harmonics. Figure 5.9 (B) shows the two dimension version the harmonics spectrum. The diffracted harmonics were the first order diffraction

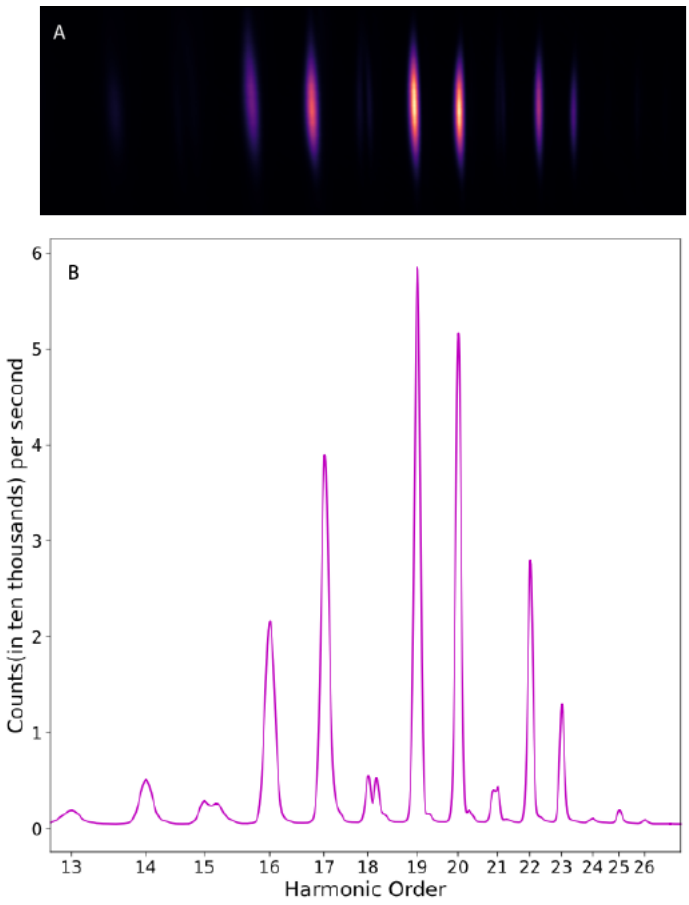

Figure 5.9 Generated circularly polarized harmonics spectrum from the MAZEL-TOV. (A) The image of the harmonic spectrum. (B) Two dimensional plot of the image with the total photon counts per second for each identified harmonic. As can be seen, there are harmonic pairs where every third harmonic is suppressed. Each pair consists of one right and one left circularly polarized beam [10, 11].

from the grating. The strongest signal was the 19^{th} harmonic which was measured about 60,000 counts per second. The harmonics came in pairs which indicate they are near circular polarization. Small peaks are shown around the main peaks. This is an indication that the driving laser beams may not have perfect circular polarization [50]. The MAZEL-TOV would need to be adjusted to better improve the circular polarization. Comparing the MAZEL-TOV and the linear spectra show that the circular harmonics have a stronger signal at lower harmonics as shown in Figure 5.10A.

These harmonics were optimized with the following parameters: laser power output of 3.62 Watts, 1000 mm focal-length lens, argon gas pressure of 11 Torr, and a medium length of 8 mm. The calcite plates were tuned to make a normal-incidence angle of $-8.33^o \pm 0.17^o$ which corresponds to about 633 ± 5.33 fsec of delay compensation which agrees within two standard deviations compared to the calculated value of 640 fsec.

The harmonics were identified using both MAZEL-TOV and linear spectra. Without the MAZEL-TOV inserted, the spectrum is a typical HHG where only the odd harmonics are generated [34] [56]. Figure 5.10A depicts the normalized linear and circular spectra. The odd harmonics of the linear spectrum is used to identify the odd harmonics of the MAZEL-TOV spectrum. An arrow pointing to the suppressed odd harmonic in Figure 5.10A must be a multiple of three. This harmonic must be the 21^{st}, 27^{th}, or 33^{rd} harmonic.

Thin metal filters were used to calibrate the harmonics. Once calibrated, the suppressed odd harmonic indicated on Figure 5.10A can be determined. We have chosen to use iron and zirconium due to their absorption edges in this region. The 21^{st}, 27^{th}, and 33^{rd} harmonics correspond to energies 33, 42, and 52 eV, respectively. Figure 5.10B plots the measured linear and circular spectra with transmission curves taken from CXRO database [12]. The iron signal should cut off just after 52.7 eV. Observation of the linear spectrum through the iron filter shows that the 27^{th} harmonic could not be the suppressed odd harmonic. The last harmonic would have an energy beyond 52.7 eV. The same would be true for the 33^{rd} harmonic. We can then conclude that the suppressed odd

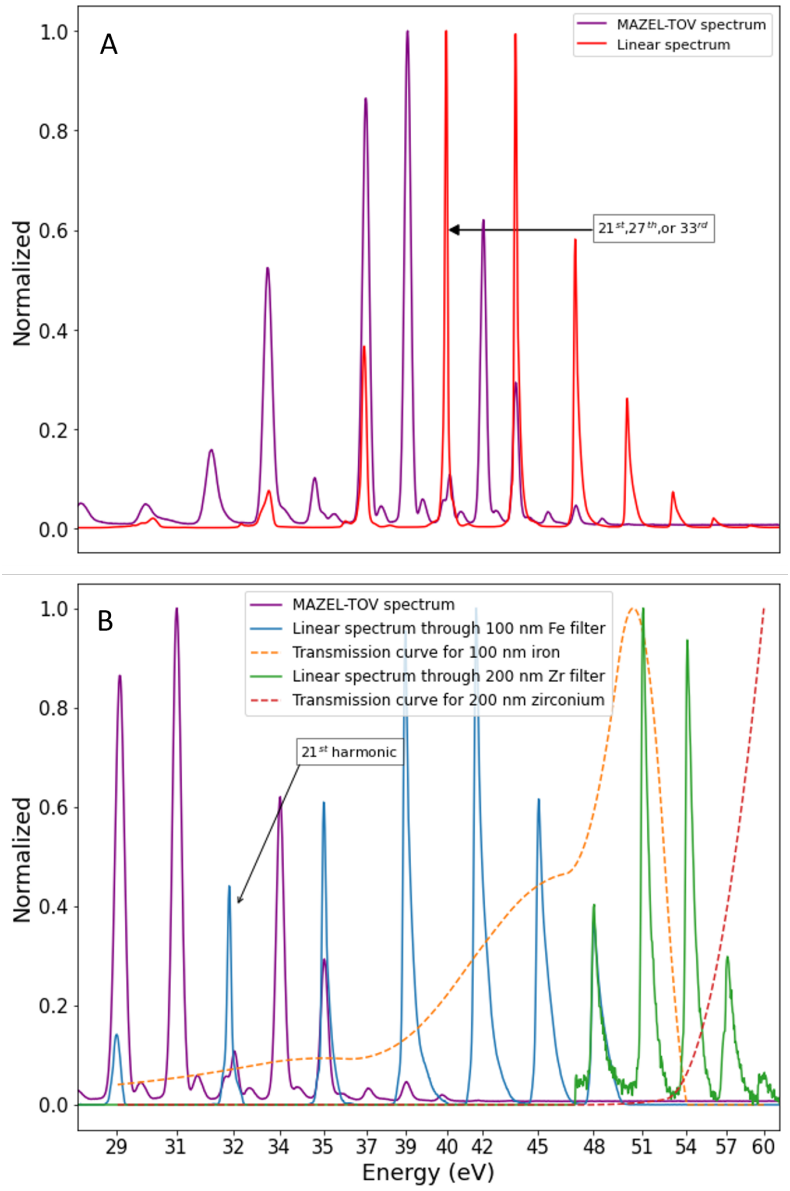

Figure 5.10 (A) Combined circular and linear spectra of the high harmonic source. The linear spectrum (red) was generated using typical high harmonic methods which only generates linearly polarized light. The circular or MAZEL-TOV spectrum (purple) shows odd and even harmonics with every third harmonic suppressed. Comparison of the two spectra reveals which of the harmonics of the circular spectrum are odd. An arrow is drawn showing a suppressed odd harmonic that must be the 21^{st}, 27^{th}, or 33^{rd} harmonic. (B) Normalized curves of circular and linear spectra with transmission curves. Data for transmission curves taken from CXRO x-ray database [12] and then interpolated to the spectra.

harmonic identified in Figure 5.10A must be the 21^{st}. We have noticed though that the last harmonic of the iron linear spectrum would be would be the 31^{st} which has a photon energy of 48.4 eV. The 33^{rd} harmonic, 51.15 eV, was not in the spectrum with the iron filter inserted. This harmonic should be the last harmonic in the spectrum according to the calculations reported on the CXRO website [12]. A reasonable explanation is that CXRO database could be off by a few electron volts making the resonant edge of iron less than 52.7 eV. Several past experiments for determining optical constants, δ and β, in the EUV showed the measured values of several materials were significantly difference than the reported values on CXRO website [57, 58].

We believe the generated harmonics are circularly polarized light. However, reflection from metallic surfaces at small grazing incidence could alter the polarization of the beam. This could be a problem for magnetic imaging. The polarization of the reflected beam is determined using Jones vectors and matrices discussed in the optics textbook from Dr. Justin Peatross and Dr. Micheal Ware [40]. The optical constants at 52.7 eV for gold is $\delta = 0.15648$ and $\beta = 0.19095$ [12]. The EUV will be at grazing incidence of 10 degrees for the toroidal mirror. The calculated ellipticity after the toroidal mirror would change from 1 to 0.78 which is significant. The actual polarization will need to be measured to observe how the mirrors affect the polarization. However, magnetic contrast imaging has been demonstrated using a toroidal grating at grazing incidence with the MAZEL-TOV [31]. This would imply that further investigation will need to be required to confirm the polarization of the circular harmonics.

5.3 Reconstruction of the Two Pinhole Diffraction

The EUV source was used to obtain a diffraction pattern from a sample for a reconstruction. I have written a reconstruction algorithm which uses error reduction, hybrid input-output, and shrinkwrap algorithms [6,44]. The images obtained were processed to ensure the python code would reconstruct.

This includes background subtraction and threshold. The sample is a set of double pinholes with a diameter of 10 microns separated by 40 microns. The double pinholes were also used to show the spatial coherence of the EUV beam. The Fresnel number was calculated by taking the ratio of the measured distance from the sample to the detector and the far-field distance, $z_{far} = object\ size/\lambda$. If $z_{far}/z_{measured} << 1$ then the sample is in the far-field regime [59].

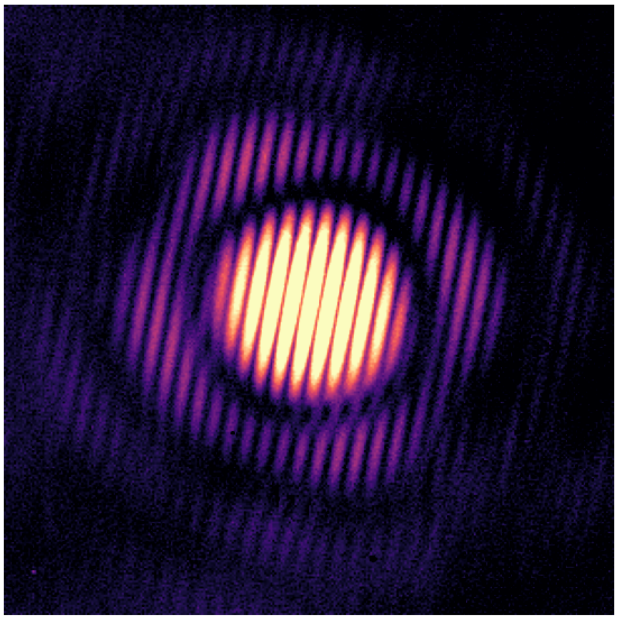

Figure 5.11 Measured diffraction signal of two 10 micron pineholes separated by a distance of 40 microns. This diffraction pattern is used to reconstruct the pinholes with CDI. The visibility of the fringes indicates that the generate 42 eV harmonics has high spatial coherence. The signal is log scaled to show the outer rings. A description of how the data was processed can be found in appendix E

We used 42 eV normal incident mirrors to focus the laser onto the pinholes. Figure 5.11 is the measured diffraction pattern taken with 10 signal exposure images with 6 minutes of exposure time on an Andor iKon-L back-thinned CCD. It is worth noting the fringe visibility of the two pinhole diffraction pattern in Figure 5.11. This indicates that the 42 eV beam has a high degree of spatial coherence. Each image was subtracted by the average of 5 backgrounds. Each of the background subtracted images was then summed together. 19.8 ± 0.1 cm was the measured distance between

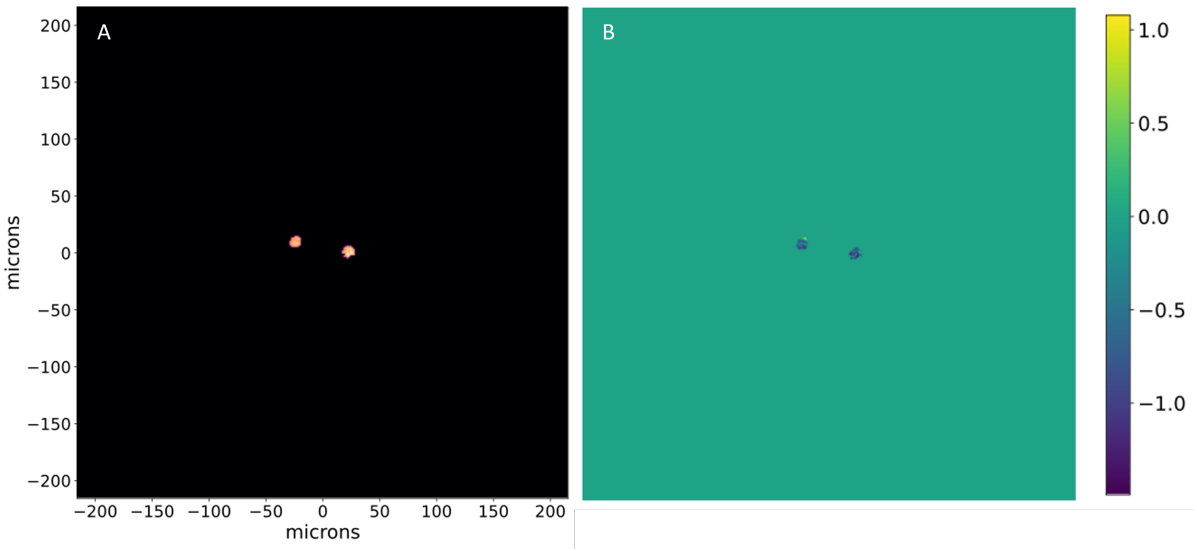

Figure 5.12 Reconstruction of the two pinhole diffraction pattern. The OS was calculated to be 7.2. (A) shows the reconstructed pinholes and (B) is the retrieved phase of the pinholes.

the sample and detector. The pixel size of the CCD is 13.5 microns. With these parameters, the oversampling was calculated to be 7.2. The far field distance for this aperture size and wavelength was calculated to be 6.62 mm which gives a Fresnel number of 0.33 which is in the Fraunhoffer regime [59].

My phase retrieval algorithm reconstructed the double pinholes from the diffraction pattern in Figure 5.11. The reconstructed image with the retrieved phase is shown in Figure 5.12. As can be seen from Figure 5.12, my algorithm was successful in reconstruction the two pinholes. There has been previous work at Los Alamos National Laboratory that has shown that reconstructions can still converge for Fresnel numbers up to 2.1 [59].

I measured the diameter and separation of the double pinholes with a microscope for comparison with the reconstructed pinholes. The measurements are show in Figure 5.13A. The reconstructed image measurements were analyzed using the FWHM of both pinholes. The reconstructed pinholes were 8.6 and 8.0 microns with a separation of 39.2 microns. The larger reconstructed pinhole

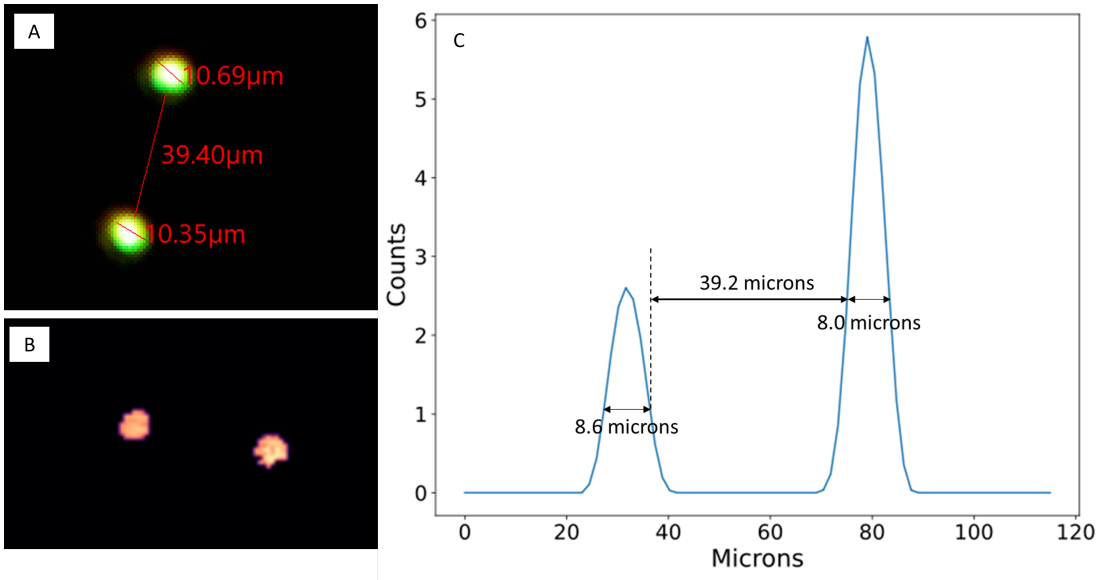

Figure 5.13 Two pinhole measurements. (A) Pinholes measured under a microscope. They are about 10 microns in diameter with 40 micron seperation. (B) Image of the reconstructed pinholes. (C) is the two dimensional plot of the reconstructed pinholes with the measured values. Measurements of the reconstructed pinholes were found by considering the FWHM of each peak. One peak is greater than the other which indicates that the right peak was more brightly illuminated by the EUV beam.

indicates that it was more illuminated by the EUV beam. Figure 5.13C shows the results of the measurements of the reconstructed pinholes. The separation was very close to the microscope measurements but the pinhole diameters were off by about 2 microns. This indicates that the oversampling of the diffraction pattern may be slightly incorrect. The reconstructed pinholes measurements are close to the measured values with the microscope. We have demonstrated that the tabletop EUV source can be used to reconstruct scattered light from a sample. In the future, we will be implementing the ptychography algorithm to reconstruct polarization sensitive samples such as magnetic domains.

Chapter 6

Conclusion

We have successfully developed a tabletop EUV source which can be used for polarization sensitive measurements such as magnetic imaging. The high harmonics have been optimized to generate 8.1 billion photons per second for the 42 eV harmonic and 1.5 billion photons per second for the 52 eV harmonic. We can still explore other parameters to improve the signal of the 42 and 52 eV harmonics. For example, we have a 2000 mm focal-length lens. A 2000 mm lens cause a beam to have very low divergence which would be a problem with the aluminum filters. We did recently obtain a beam splitter mechanism that would allow the EUV harmonics to pass through to the sample while blocking the IR beam. This will allow for the longer focal-length lens which could lead to better signal of harmonics.

Generating circularly polarized light has also been successful. The 52 eV harmonic still needs to be optimized with the MAZEL-TOV inserted. Higher harmonics required more laser power which is a problem for the aluminum filters. The beam splitter is able to handle more power compared to the filters. We did not have the beam splitter available when we were performing the experiment. Achieving a better signal of the circularly polarized 52.7 eV harmonic is necessary to begin imaging of magnetic domains of iron nanoparticles.

We have not directly measured the polarization of the EUV harmonics from the MAZEL-TOV

spectrum. We are currently assuming it is circularly polarized because it has been theoretically predicted and experimentally confirmed in previous publications [10, 11, 31, 32, 49, 50, 55]. For example, the Oren Cohen group used the MAZEL-TOV to perform reconstructions of magnetic samples using holography [31]. Further work is needed to confirm that we are generating circularly polarized harmonics. The circular polarization can be confirmed using the 52.7 eV circular harmonic to obtain a diffracted image of a magnetic thin film (probably iron). If the light was circularly polarized, we would see a speckle ring diffraction pattern (see Figure 6.1) from the resonantly illuminated sample when the diffraction from the right and left polarizations were subtracted from one another [1, 55]. This would indicate that the generated EUV light is circularly polarized. Identifying the harmonics in the linear and circular spectra has revealed that the resonant edge of iron did not completely agree with the values calculated on the CXRO website. Further work is needed to confirm the resonant edge of iron near 52.7 eV.

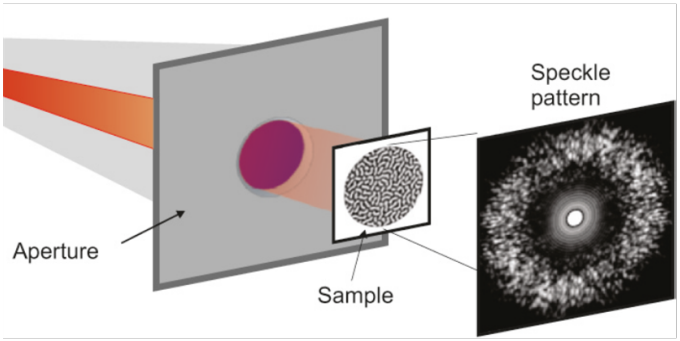

Figure 6.1 Diagram of diffraction from a magnetic sample. The diffraction pattern would contain a dim circular speckle pattern surrounding the central diffraction pattern. The speckle pattern contains information of the magnetic domains. This image was altered and taken from [1].

The EUV source has been successfully used to reconstruct a double pinhole sample from a recorded diffraction pattern. The double pinhole diffraction also indicates that the source generates highly coherent EUV laser beams. We will use other reconstruction algorithms such as ptychography to reconstruct magnetic domains.

Appendix A

Physical Constants and Useful Relations

Planck's constant: $\hbar = 6.582 \times 10^{-16} eV \cdot s$

Mass of electron: $m_e = 9.981 \times 10^{-31} kg$

Speed of light: $c = 3.00 \times 10^{8} m/s$

Vacuum permittivity: $\varepsilon_0 = 8.854 \times 10^{-12} F/m$

$1239.842 nm \cdot eV = \lambda \cdot Energy(\lambda)$

Appendix B

Phase Retrieval Algorithms

Generic algorithm of CDI used in this thesis is given as equation B.1. The modulus of the diffracted electric field at the detector is found by taking the square root of the measured intensity. Next, a random phase $[\phi_k(u)]$, is multiplied to the electric field $[|G'_k(u)|]$. The inverse discrete fast Fourier transform (FFT) back propagates the electric field $[g'_k(x)]$ to the domain of the object. Constraints are applied to the estimated object. The constraints adjust the phase $[\theta_{k+1}(x)]$ for the electric field, in the sample's plane. Next, a FFT is used to propagate the constrained electric field back to the detector plane $[G_k(u)]$. By comparing the amplitude of the altered electric field with the original square root of the measured intensity $[|F(u)|]$, we can determine the error of our current 'retrieved' diffracted field. We then apply another constraint by replacing the retrieved current iteration electric field amplitude with the square root of the measured intensity and multiplying it by the new phase. This is repeated until the algorithm has converged and the phase is retrieved.

$$
\begin{aligned}
G_k(u) &= |G_k(u)|exp[i\phi_k(u)] = \mathscr{F}[g_k(x)] \\
G'_k(u) &= |F(u)|exp[i\phi_k(u)] \\
g'_k(x) &= |g'_k(x)|exp[i\theta'_k(x)] = \mathscr{F}^{-1}[G'_k(u)] \\
g_{k+1} &= |f(x)|exp[i\theta_{k+1}(x)] = |f(x)|exp[i\theta'_k(x)]
\end{aligned}
\tag{B.1}
$$

B.1 Error Reduction Algorithm

The error reduction algorithm is the most simple [6, 60]. The constraints are the compact support, positive constraint, and real object. Compact support restricts the object to exist in a particular region and determines the oversampling together with the wavelength, detector pixel size, and sample to detector distance. The positivity constraint forces all the values to be positive of the amplitude. The real object only applies when the object does not have absorption of light. These constraints are applied according to equation B.2 where a specifies the region where x should exist [6].

$$
g_{k+1}(x) = \begin{cases} g'_k(x) & x \in a \\ 0 & x \notin a \end{cases}
\tag{B.2}
$$

B.2 Hybrid Input-Output

The hybrid input-output algorithm is similar to the error reduction algorithm except that the constraints are not as restrictive (see equation B.3) [6, 61]. A problem with the error reduction algorithm is it tends to stagnant and converges very slowly. The stagnant is caused by minimum errors in the computed in the algorithm. There are several minimums but only one of them is the correct one. β represents the strength of the restriction when x violates the conditions. The hybrid input-output speeds up the reconstruction. Typically, hybrid input-output is combined with the error

reduction method. Notice that when $\beta = 1$ the hybrid input-output is reduced to the error reduction algorithm.

$$g_{k+1}(x) = \begin{cases} g'_k(x) & x \in a \\ g'_k(x) - \beta g'_k(x) & x \notin a \end{cases} \tag{B.3}$$

B.3 Shrinkwrap

The shrinkwrap algorithm build upon the hybrid input-output algorithm [44]. Complex objects can be difficult to reconstruct because the support constraint may not be tight enough for the hybrid input-output to work properly. The shrinkwrap algorithm adjusts the support constraint as the hybrid input-output iterates. After several iterations of hybrid input-output, a Gaussian of width *sigma* is used to smooth out the updated object. A 20% threshold is then applied to the object and forms a new compact support which is used for further hybrid input-outputs. This is repeats several times with *sigma* decreasing until the compact support wraps around the region where the object exists. Thus the name shrinkwrap. This combined with the hybrid input-output and error reduction causes the algorithm to converge quickly with high resolution.

B.4 Code Used for Reconstruction of Images for this Thesis

Below is the example of my code which reconstructs a sample from a diffraction pattern. The code includes error reduction, hybrid input-output, and shrinkwrap.

```
import numpy as np
import matplotlib.pyplot as plt
from scipy.ndimage import gaussian_filter
from tifffile import imsave
```

```
"""upload numpy array that represents an image"""
data = np.load("filename")
"""parameters"""
N = len(data)                       # Length of data array
z = .198                            # Distance between sample and detector
lamda = 800e-9/27                   # Wavelength of light
pdet = 13.6e-6                      # Pixel length in detector
lendet = len(data)*pdet             # Length of the detector
lensampledomain = z*lamda/pdet      # length of sample domain
psample = lensampledomain/N         # Pixel length in sample domain
OS = z*lamda/pdet/50e-6
"""Create Mask based on oversampling"""
X = np.arange(-(lensampledomain+psample)/2,
        (lensampledomain-psample)/2, psample)
Y = X
x,y = np.meshgrid(X,Y)
a = z*lamda/pdet/OS # size of the initial mask using oversampling
mask = np.zeros((N,N))
mask[(np.abs(x+y)+np.abs(x-y))<= a]=1
"""Prepare data"""
E = np.fft.ifftshift(np.sqrt(data))
np.random.seed(12345)
G = E*np.exp(1j*2*np.pi*np.random.rand(*data.shape))
```

```
k = 2  #number of shrinkwraps
beta = 0.9  #beta parameter for HIO algorithm
sigma = np.linspace(1,k,k)   #sigmas for shrinkwrap
#Thresholds for shrinkwrap
threshold = np.flip(np.linspace(0.05,0.2,k))

while k > 0:
    #ER iterations
    for i in range(1,11):
        if i % 10 == 0:
            print('Step',i, "ER iteration")
        g = np.fft.ifft2(G) #inverse fourier transform
        #positivity and compact support
        constraints = np.logical_or(np.logical_and(g<0,mask)
                ,np.logical_not(mask))
        gp = g
        gp[constraints]=0 #Apply contraints on gp
        Gp = np.fft.fft2(gp) # fourier transform
        G = E*np.exp(1j*np.angle(Gp)) #fourier constraint
    #HIO iterations
    for j in range(1,31):
        if j % 10 == 0:
            print('Step',j,'HIO iteration')
        g = np.fft.ifft2(G)
        g_p = gp
```

```
        constraints = np.logical_or(np.logical_and(g<0,mask)
                ,np.logical_not(mask))
        gp = g
        gp[constraints]= g_p[constraints]-beta*g[constraints]
        Gp = np.fft.fft2(gp)
        G = E*np.exp(1j*np.angle(Gp))
    mask = gaussian_filter(np.abs(gp),sigma[k-1])
    mask = mask/np.max(mask)
    mask[mask>=0.2]=1
    mask[mask<threshold[k-1]]=0
    k -= 1
for i in range(1,201):
        if i % 10 == 0:
            print('Step',i, "ER iteration")
        g = np.fft.ifft2(G)
        constraints = np.logical_or(np.logical_and(g<0,mask)
                ,np.logical_not(mask))
        gp = g
        gp[constraints]=0
        Gp = np.fft.fft2(gp)
        G = E*np.exp(1j*np.angle(Gp))
```

Appendix C

EUV Mirrors Reflection Curves

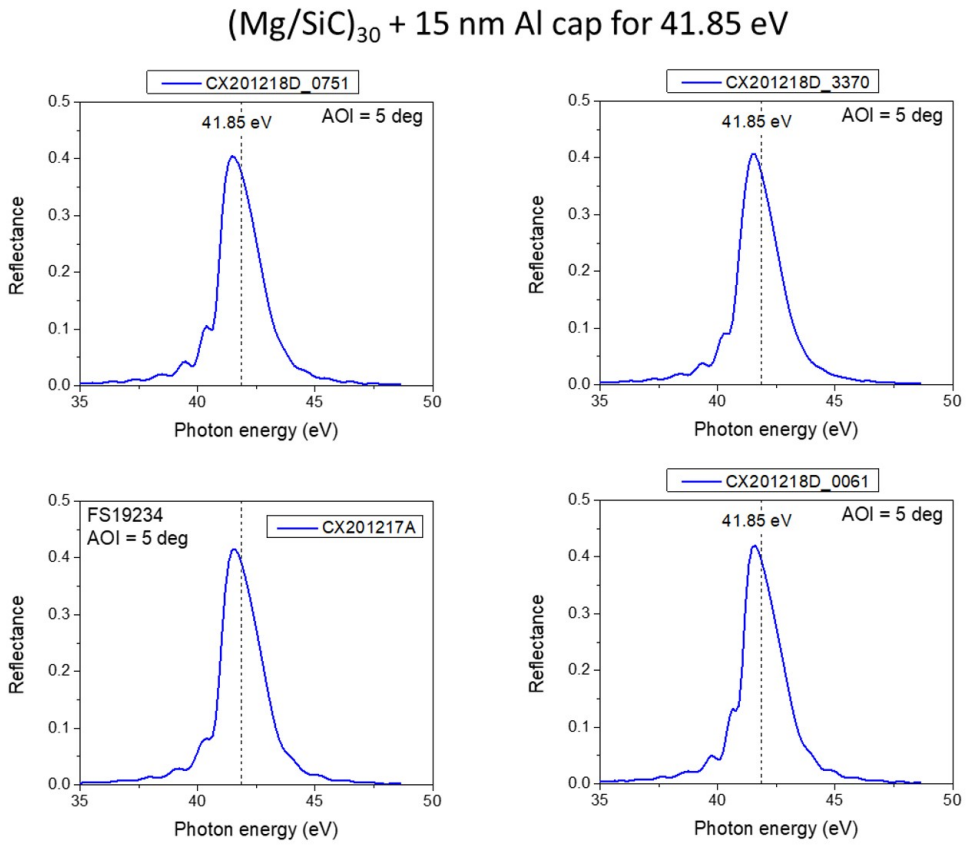

Figure C.1 Measured reflections of the 42 eV mirrors.

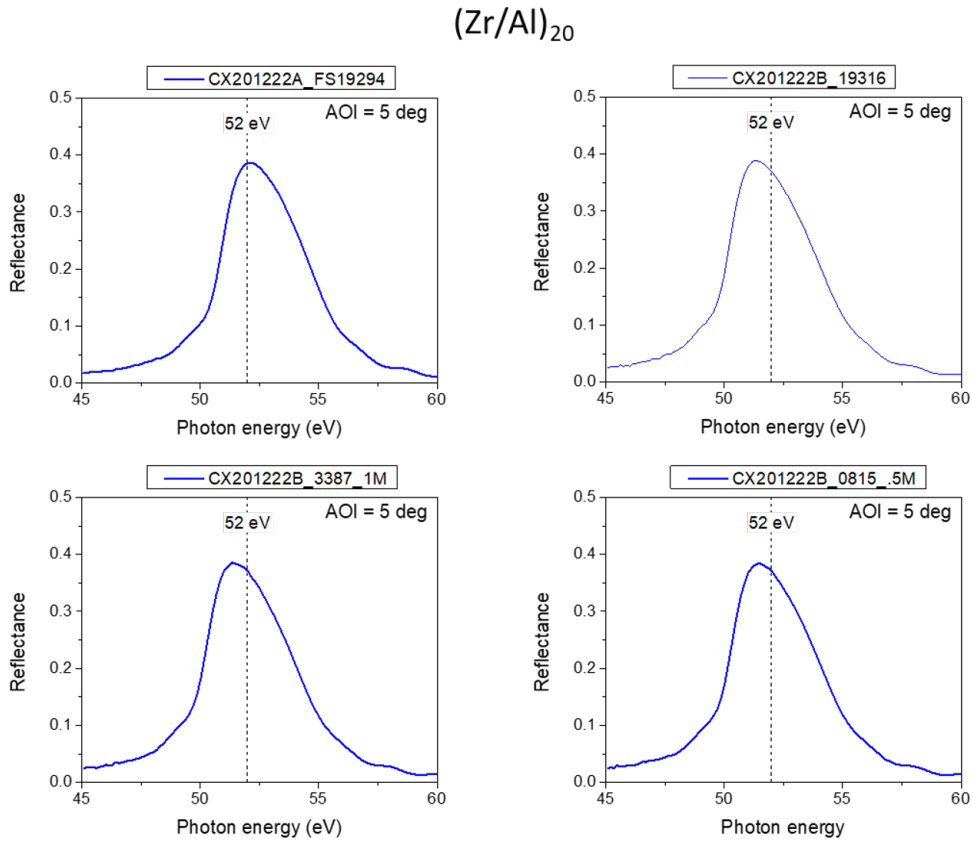

Figure C.2 Measured reflections of 52 eV mirrors.

Appendix D

Transmission Tables for Aluminum Filters

Aluminum Filter Transmission for 42 eV Light				
Filter Configuration	Combination	Photons(in millions) per second for select pressures		
		9.5 Torr	10.8 Torr	8.4 Torr
1	1-0.2 then 1-0.1	785	1087	535
2	1-0.1 then 1-0.2	738	911	499
3	2-0.1	1775	1933	1145
4	2-0.2	343	417	198
Comparing the configurations				Average
Compare 1 and 3	0.44 ± 0.01	0.47 ± 0.01	0.01 ± 0.01	0.46 ± 0.01
Compare 2 and 3	0.42 ± 0.06	0.56 ± 0.06	0.43 ± 0.06	0.47 ± 0.05
Compare 4 and 3	0.19 ± 0.02	0.22 ± 0.02	0.17 ± 0.02	0.19 ± 0.02
Compare 4 and 1	0.44 ± 0.03	0.38 ± 0.03	0.37 ± 0.03	0.40 ± 0.02

Table D.1 Filter transmission for 42 eV light. This is used to compare how much light is transmitted with different configurations of filters. The combinations such as 1-0.2 then 1-0.1 read one 0.2 micron filter then one 0.1 micron filter. When the CCD camera was saturated, a thicker filter was used to prevent saturation. This data table help estimate how many photons per second hit the CCD camera if thinner filters were used. This was primarily used to optimization of HHG.

Aluminum Filter Transmission for 52 eV Light				
Filter Configuration	Combination	Photons(in millions) per second for select pressures		
		9.5 Torr	10.8 Torr	8.4 Torr
1	1-0.2 then 1-0.1	49	46	29
2	1-0.1 then 1-0.2	43	42	37
3	2-0.1	109	108	90
4	2-0.2	22	21	17
Comparing the configurations				Average
Compare 1 and 3	0.39 ± 0.03	0.39 ± 0.03	0.32 ± 0.03	0.37 ± 0.02
Compare 2 and 3	0.45 ± 0.02	0.42 ± 0.02	0.41 ± 0.02	0.43 ± 0.01
Compare 4 and 3	0.21 ± 0.01	0.19 ± 0.01	0.18 ± 0.01	0.19 ± 0.01
Compare 4 and 1	0.45 ± 0.05	0.46 ± 0.05	0.57 ± 0.05	0.49 ± 0.04

Table D.2 Filter transmission for 52 eV light. This is used to compare how much light is transmitted with different configurations of filters. The combinations such as 1-0.2 then 1-0.1 read one 0.2 micron filter then one 0.1 micron filter. When the CCD camera was saturated, a thicker filter was used to prevent saturation. This data table help estimate how many photons per second hit the CCD camera if thinner filters were used. This was primarily used to optimization of HHG.

Appendix E

Processing Two Pinhole Diffraction Pattern and Reconstruction

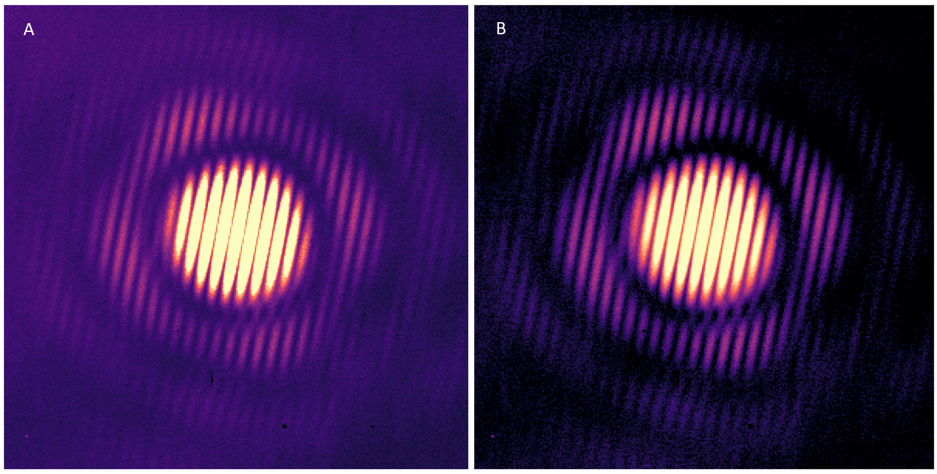

Figure E.1 Images of the data (A) before and (B) after processing preparatory for reconstruction. There is a background gradient coming from the scattered EUV beam in image (A) which needed to be removed for CDI to work properly.

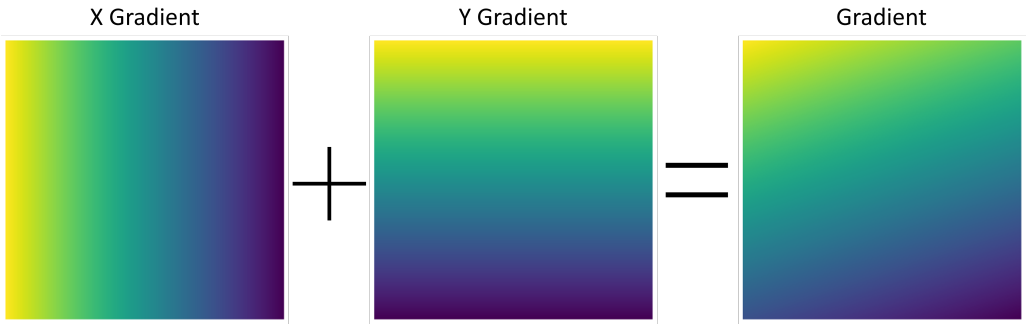

Figure E.2 Linear threshold created using a combination of X and Y gradient images. This was used to threshold the pinhole data to minimize the gradient noise. The values of the Y gradient are three times more than the X gradient. The linear gradient still needed to be combined with a flat threshold else another gradient background is formed in the image.

Bibliography

[1] J. Stöhr and H. C. Siegmann, in *Magnetism: From Fundamentals to Nanoscale Dynamics* (Springer, Berlin, Heidelberg, 2006).

[2] P. B. Corkum, "Plasma perspective on strong field multiphoton ionization," Phys. Rev. Lett. **71,** 1994–1997 (1993).

[3] H. Kapteyn, M. Murnane, and I. Christov, "Extreme Nonlinear Optics: Coherent X rays from Lasers," Physics Today **58,** 39–44 (2005).

[4] C. Ding, W. Xiong, T. Fan, D. D. Hickstein, T. Popmintchev, X. Zhang, M. Walls, M. M. Murnane, and H. C. Kapteyn, "High flux coherent super-continuum soft X-ray source driven by a single-stage, 10mJ, Ti:sapphire amplifier-pumped OPA," Opt. Express **22,** 6194–6202 (2014).

[5] R. A. Bartels, A. Paul, H. Green, H. C. Kapteyn, M. M. Murnane, S. Backus, I. P. Christov, Y. Liu, D. Attwood, and C. Jacobsen, "Generation of Spatially Coherent Light at Extreme Ultraviolet Wavelengths," Science **297,** 376–378 (2002).

[6] J. R. Fienup, "Phase retrieval algorithms: a comparison," Appl. Opt. **21,** 2758–2769 (1982).

[7] R. Sandberg, "Closing the gap to the diffraction limit: Near wavelength limited tabletop soft x-ray coherent diffractive imaging," PhD Dissertation (2009).

[8] S. LTD., "Toroidal Mirrors,", 2020, last accessed 23 February 2022. http://www.standaphotonics.com/off-axis-mirrors/toroidal-mirrors.php.

[9] E. Optics, "Delay compensation plates,", 2021, last accessed 28 February 2022. https://eksmaoptics.com/femtoline-components/femtoline-nonlinear-laser-crystals/group-velocity-delay-compensation-plates/.

[10] O. Kfir, E. Bordo, G. Ilan Haham, O. Lahav, A. Fleischer, and O. Cohen, "In-line production of a bi-circular field for generation of helically polarized high-order harmonics," Applied Physics Letters **108,** 211106 (2016).

[11] A. Fleischer, O. Kfir, T. Diskin, P. Sidorenko, and O. Cohen, "Spin angular momentum and tunable polarization in high-harmonic generation," Nature Photonics **8,** 543–549 (2014).

[12] E. Gullikson, "X-Ray Interactions With Matter,", 2010, last accessed 18 February 2022.

[13] D. Attwood and A. Sakdinawat, *X-Rays and Extreme Ultraviolet Radiation: Principles and Applications*, 2nd ed. (Cambridge University Press, 2017).

[14] V. Baltz, A. Manchon, M. Tsoi, T. Moriyama, T. Ono, and Y. Tserkovnyak, "Antiferromagnetic spintronics," Rev. Mod. Phys. **90,** 15005 (2018).

[15] A. V. Kimel, A. Kirilyuk, P. A. Usachev, R. V. Pisarev, A. M. Balbashov, and T. Rasing, "Ultrafast non-thermal control of magnetization by instantaneous photomagnetic pulses," Nature **435,** 655–657 (2005).

[16] D. Fausti, R. I. Tobey, N. Dean, S. Kaiser, A. Dienst, M. C. Hoffmann, S. Pyon, T. Takayama, H. Takagi, and A. Cavalleri, "Light-Induced Superconductivity in a Stripe-Ordered Cuprate," Science **331,** 189–191 (2011).

[17] J. Kortright, D. Awschalom, J. Stöhr, S. Bader, Y. Idzerda, S. Parkin, I. K. Schuller, and H.-C. Siegmann, "Research frontiers in magnetic materials at soft X-ray synchrotron radiation facilities," Journal of Magnetism and Magnetic Materials **207,** 7–44 (1999).

[18] F. Nolting *et al.*, "Direct observation of the alignment of ferromagnetic spins by antiferromagnetic spins," Nature **405,** 767–769 (2000).

[19] S. Eisebitt, J. Lüning, W. F. Schlotter, M. Lörgen, O. Hellwig, W. Eberhardt, and J. Stöhr, "Lensless imaging of magnetic nanostructures by X-ray spectro-holography," Nature **432,** 885–888 (2004).

[20] T. Popmintchev, M.-C. Chen, P. Arpin, M. M. Murnane, and H. C. Kapteyn, "The attosecond nonlinear optics of bright coherent X-ray generation," Nature Photonics **4,** 822–832 (2010).

[21] T. Popmintchev, "Tunable ultrafast coherent light in the soft and hard X-ray regions of the spectrum: Phase matching of extreme high-order harmonic generation," PhD Dissertation (2010).

[22] A. Lytle, "Phase Matching and Coherence of High-Order Harmonic Generation in Hollow Waveguides," PhD Dissertation (2008).

[23] R. L. Sandberg, Z. Huang, R. Xu, J. A. Rodriguez, and J. Miao, "Studies of Materials at the Nanometer Scale Using Coherent X-Ray Diffraction Imaging," JOM **65,** 1208–1220 (2013).

[24] J. Miao, R. L. Sandberg, and C. Song, "Coherent X-Ray Diffraction Imaging," IEEE Journal of Selected Topics in Quantum Electronics **18,** 399–410 (2012).

[25] J. Miao, T. Ishikawa, I. K. Robinson, and M. M. Murnane, "Beyond crystallography: Diffractive imaging using coherent x-ray light sources," Science **348,** 530–535 (2015).

[26] R. L. Sandberg, D. A. Raymondson, C. L. o vorakiat, A. Paul, K. S. Raines, J. Miao, M. M. Murnane, H. C. Kapteyn, and W. F. Schlotter, "Tabletop soft-x-ray Fourier transform holography with 50 nm resolution," Opt. Lett. **34,** 1618–1620 (2009).

[27] D. F. Gardner *et al.*, "Subwavelength coherent imaging of periodic samples using a 13.5nm tabletop high-harmonic light source," Nature Photonics **11,** 259–263 (2017).

[28] L. Loetgering, S. Witte, and J. Rothhardt, "Advances in laboratory-scale ptychography using high harmonic sources," Opt. Express **30,** 4133–4164 (2022).

[29] P. D. Baksh *et al.*, "Quantitative and correlative extreme ultraviolet coherent imaging of mouse hippocampal neurons at high resolution," Science Advances **6,** eaaz3025 (2020).

[30] R. M. Karl *et al.*, "Full-field imaging of thermal and acoustic dynamics in an individual nanostructure using tabletop high harmonic beams," Science Advances **4,** eaau4295 (2018).

[31] O. Kfir *et al.*, "Nanoscale magnetic imaging using circularly polarized high-harmonic radiation," Science Advances **3,** eaao4641 (2017).

[32] O. Kfir *et al.*, "Generation of bright phase-matched circularly-polarized extreme ultraviolet high harmonics," Nature Photonics **9,** 99–105 (2015).

[33] J. Peatross, J. Zhou, I. Christov, A. Rundquist, M. M. Murnane, and H. C. Kapteyn, "High-order harmonic generation with a 25 femtosecond laser pulse," In *Proceedings of 4th Conference on Super Intense Laser-Atom Physics (SILAP IV, Moscow, Russia, August 1995)*, H. Muller and M. V. Fedorov, eds., High Technology **13,** 455–466 (Kluwer Academic Publishers, Dordrecht/Boston/London, 1996).

[34] E. Constant, D. Garzella, P. Breger, E. Mével, C. Dorrer, C. Le Blanc, F. Salin, and P. Agostini, "Optimizing High Harmonic Generation in Absorbing Gases: Model and Experiment," Phys. Rev. Lett. **82,** 1668–1671 (1999).

[35] E. Takahashi, Y. Nabekawa, T. Otsuka, M. Obara, and K. Midorikawa, "Generation of highly coherent submicrojoule soft x rays by high-order harmonics," Phys. Rev. A **66,** 021802 (2002).

[36] E. Takahashi, Y. Nabekawa, and K. Midorikawa, "Generation of 10-μJ coherent extreme-ultraviolet light by use of high-order harmonics," Opt. Lett. **27,** 1920–1922 (2002).

[37] M. V. Ammosov, N. B. Delone, and V. P. Krainov, "Tunnel ionization of complex atoms and atomic ions in an electromagnetic field," Sov. Phys. JETP **64,** 1191–1194 (1986).

[38] A. L'Huillier, K. J. Schafer, and K. C. Kulander, "Theoretical aspects of intense field harmonic generation," Journal of Physics B: Atomic, Molecular and Optical Physics **24,** 3315–3341 (1991).

[39] J. L. Krause, K. J. Schafer, and K. C. Kulander, "High-order harmonic generation from atoms and ions in the high intensity regime," Phys. Rev. Lett. **68,** 3535–3538 (1992).

[40] J. Peatross and M. Ware, *Physics of Light and Optics* (optics.byu.edu, Provo, Utah, 2015).

[41] T. Ditmire, E. T. Gumbrell, R. A. Smith, J. W. G. Tisch, D. D. Meyerhofer, and M. H. R. Hutchinson, "Spatial Coherence Measurement of Soft X-Ray Radiation Produced by High Order Harmonic Generation," Phys. Rev. Lett. **77,** 4756–4759 (1996).

[42] C. Lyngå, M. B. Gaarde, C. Delfin, M. Bellini, T. W. Hänsch, A. L' Huillier, and C.-G. Wahlström, "Temporal coherence of high-order harmonics," Phys. Rev. A **60,** 4823–4830 (1999).

[43] E. Hecht, in *Optics*, 4th ed., A. Black, ed., (Pearson Education, Inc, 1301 Sansome St., San Francisco, CA, 2002).

[44] S. Marchesini, H. He, H. N. Chapman, S. P. Hau-Riege, A. Noy, M. R. Howells, U. Weierstall, and J. C. H. Spence, "X-ray image reconstruction from a diffraction pattern alone," Phys. Rev. B **68,** 140101 (2003).

[45] A. M. Maiden and J. M. Rodenburg, "An improved ptychographical phase retrieval algorithm for diffractive imaging," Ultramicroscopy **109,** 1256–1262 (2009).

[46] O. Instruments, "CCD, sCMOS EMCCD Cameras for X-ray and EUV Detection," https://andor.oxinst.com/products/cameras-for-x-ray-euv-electron-and-neutron-detection (Accessed March 26, 2022).

[47] ARWoptical, "Toroidal Mirrors," http://arwoptical.com/toromir.html (Accessed March 26, 2022).

[48] S. Backus, C. G. Durfee, M. M. Murnane, and H. C. Kapteyn, "High power ultrafast lasers," Review of Scientific Instruments **69,** 1207–1223 (1998).

[49] S. Long, W. Becker, and J. K. McIver, "Model calculations of polarization-dependent two-color high-harmonic generation," Phys. Rev. A **52,** 2262–2278 (1995).

[50] T. Fan *et al.*, "Bright circularly polarized soft X-ray high harmonics for X-ray magnetic circular dichroism," Proceedings of the National Academy of Sciences **112,** 14206–14211 (2015).

[51] R. W. Boyd, "Nonlinear Optics (Fourth Edition)," in *Nonlinear Optics (Fourth Edition)*, fourth edition ed., R. W. Boyd, ed., (Academic Press, 2020), pp. 65–135.

[52] R. Budriunas, "Collinear Setup for Two-Color High Harmonic Generation,", 2013.

[53] M. N. Polyanskiy, "Refractive index database,", 2022, accessed on 2022-01-17.

[54] W. F. Schlotter, "Lensless Fourier transform holography with soft x-rays," PhD Dissertation (2007).

[55] D. D. Hickstein *et al.*, "Non-collinear generation of angularly isolated circularly polarized high harmonics," Nature Photonics **9,** 743–750 (2015).

[56] O. E. Alon, V. Averbukh, and N. Moiseyev, "Selection Rules for the High Harmonic Generation Spectra," Phys. Rev. Lett. **80,** 3743–3746 (1998).

[57] N. F. Brimhall, A. B. Grigg, R. S. Turley, and D. D. Allred, "Thorium dioxide thin films in the extreme ultraviolet," In *Advances in X-Ray/EUV Optics, Components, and Applications*, A. M. Khounsary and C. Morawe, eds.,**6317,** 262 – 273 (SPIE, 2006).

[58] J. Rebellato, E. Meltchakov, R. Soufli, S. D. Rossi, X. Zhang, F. Auchère, and F. Delmotte, "Analyses of tabulated optical constants for thin films in the EUV range and application to solar physics multilayer coatings," In *Advances in Optical Thin Films VI*, M. Lequime, H. A. Macleod, and D. Ristau, eds.,**10691,** 200 – 215 (SPIE, 2018).

[59] B. A. Pound, J. L. Barber, K. Nguyen, M. C. Tyson, and R. L. Sandberg, "Near-field limitations of Fresnel-regime coherent diffraction imaging," Phys. Rev. B **96,** 54104 (2017).

[60] R. W. Gerchberg and W. O. Saxton, "A Practical Algorithm for the Determination of Phase from Image and Diffraction Plane Pictures," Optik **35,** 237–246 (1972).

[61] J. R. Fienup, "Iterative Method Applied To Image Reconstruction And To Computer-Generated Holograms," Optical Engineering **19,** 297 – 305 (1980).